FY2014 FES Theory & Simulation Performance Target
Final Report

Guoyong Fu, Robert Budny, Nikolai Gorelenkov, Francesca Poli, PPPL
Yang Chen, University of Colorado
Joseph McClenaghan, Zhihong Lin, University of California, Irvine
Don Spong, Oak Ridge National Laboratory
Eric Bass, University of California, San Diego
Ron Waltz, General Atomics, San Diego

October 14, 2014

1. Introduction

We report here the work done for the FY14 OFES Theory Performance Target as given below:

"***Understanding alpha particle confinement in ITER, the world's first burning plasma experiment, is a key priority for the fusion program. In FY 2014, determine linear instability trends and thresholds of energetic particle-driven shear Alfvén eigenmodes in ITER for a range of parameters and profiles using a set of complementary simulation models (gyrokinetic, hybrid, and gyrofluid). Carry out initial nonlinear simulations to assess the effects of the unstable modes on energetic particle transport***".

In the past year (FY14), a systematic study of the alpha-driven Alfven modes in ITER has been carried out jointly by researchers from six institutions involving seven codes including the transport simulation code TRANSP (R. Budny and F. Poli, PPPL), three gyrokinetic codes: GEM (Y. Chen, Univ. of Colorado), GTC (J. McClenaghan, Z. Lin, UCI), and GYRO (E. Bass, R. Waltz, UCSD/GA), the hybrid code M3D-K (G.Y. Fu, PPPL), the gyro-fluid code TAEFL (D. Spong, ORNL), and the linear kinetic stability code NOVA-K (N. Gorelenkov, PPPL). A range of ITER parameters and profiles are specified by TRANSP simulation of a hybrid scenario case and a steady state scenario case. Based on the specified ITER equilibria linear stability calculations are done to determine the stability boundary of alpha-driven high-n TAEs using the five initial value codes (GEM, GTC, GYRO, M3D-K, and TAEFL) and the kinetic stability code (NOVA-K). Both the effects of alpha particles and beam ions have been considered. Finally the effects of the unstable modes on energetic particle transport have been explored using GEM and M3D-K.

The report is organized as following. Sec. 2 presents briefly the main results of this work. Sec. 3 presents TRANSP simulation results of ITER profiles. Sec. 4 presents

linear simulation results of energetic particle-driven TAEs in ITER. Sec. 5 presents nonlinear simulation results. Finally a summary is given in Sec. 6.

2. Main results

The work started with specification of a range of ITER parameters and profiles by carrying out TRANSP simulation of an ITER hybrid operation scenario case and an ITER steady state operation scenario case. The hybrid case corresponds to the ITER operation scenario with a q profile nearly flat in the core of plasma and the central q value of q(0)=1.2. The steady state case corresponds to the ITER operation scenario with a strongly reversed q profile and the minimum q value of q_{min}=1.8. Linear stability simulations of alpha particle-driven Alfven modes have been carried out based on the specified ITER parameters and profiles. Six different codes are used including three gyrokinetic codes, GEM GTC and GYRO, as well as the hybrid code M3D-K, the gyro-fluid code TAEFL, and the linear kinetic stability code NOVA-K. Both alpha particle drive and beam ion drive have been considered.

With alpha particle drive alone, the results of GEM and GYRO show that the growth rate of alpha-driven TAE is maximized around n=20 for both ITER cases. The results of the n=19 mode obtained with the six codes are compared in details. Table 1 and Fig. 1 compare the calculated normalized mode frequency ω/ω_A, the linear growth rate γ/ω_A, the mode number of the largest poloidal harmonic m_{max}, the radius of the mode peak r_{max}, the stability threshold in on-axis alpha particle beta $\beta_{\alpha,crit}$, and the 2D mode structure for the hybrid case. The corresponding comparison for the steady state case is shown in Table 2 and Fig. 2.

Table 1: comparison of calculated mode frequency, growth rate, the poloidal mode number with maximum amplitude, the radius of mode peak, and the critical alpha beta for the hybrid case.

Hybrid	ω/ω_A	γ/ω_A	m_{max}	r_{max}	$\beta_{\alpha,crit}$
GEM	0.34	0.021	27	0.5	2.0%
GTC	0.29	0.01	28	0.5	1.0%
GYRO	0.33	0.04	28	0.5	1.3%
M3D-K	0.29	0.01	27	0.44	3.5%
TAEFL	0.38	0.02	25	0.35	2.0%
NOVA-K	0.30	0.016	26	0.5	3.1%

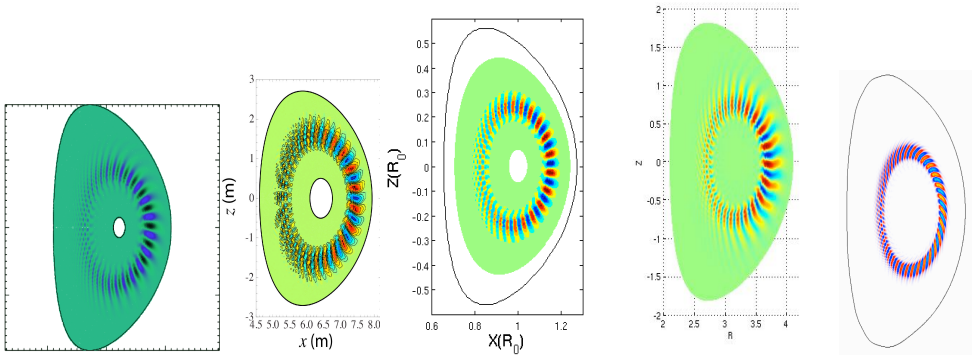

Fig. 1 Comparison of 2D mode structure of n=19 TAE obtained by GEM, GYRO, GTC, M3D-K, and TAEFL (from left to right) for the hybrid case.

Table 2: Comparison of calculated mode frequency, growth rate, the poloidal mode number with maximum amplitude, the radius of mode peak, and the critical alpha beta for the steady state case.

Steady state	ω/ω_A	γ/ω_A	m_{max}	r_{max}	$\beta_{\alpha,crit}$
GEM	0.35	0.065	39	0.6	0.7%
GTC	0.35	0.03	35	0.43	0.7%
GYRO	0.35	0.03	38	0.6	0.9%
M3D-K	0.17	0.09	38	0.52	1.0%
TAEFL	0.25	0.02	35	0.45	0.8%
NOVA-K	0.22	Stable	34	0.45	3.0%

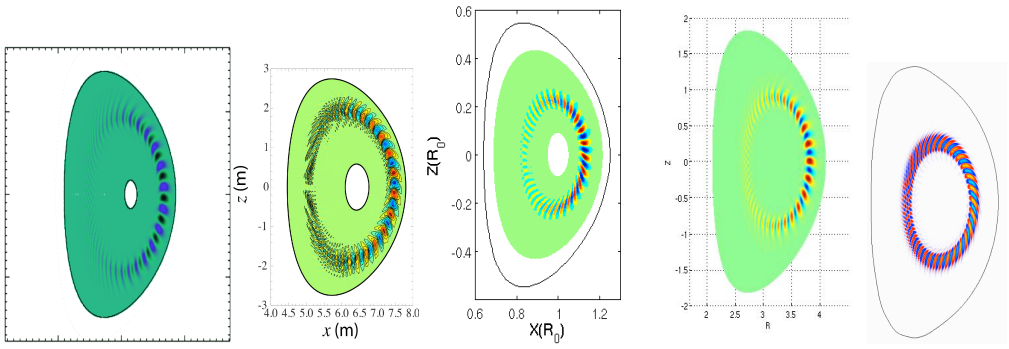

Fig. 2 Comparison of 2D mode structure of n=19 TAE calculated by GEM, GYRO, GTC, M3D-K, and TAEFL (from left to right) for the steady sate case.

Comparing the calculated mode frequencies and mode structures we observe that the results are mostly similar. The mode frequencies are around ω/ω_A=0.3. The mode structures peak near mid-radius r/a~0.5 with strong ballooning features. It should be pointed out that the mode structures calculated by the ideal MHD code NOVA are quite different from those of other codes with energetic particle drive indicating that a non-perturbative treatment of the alpha-driven TAEs is needed for the ITER cases considered here.

Comparing the calculated alpha beta thresholds for the two ITER cases, we observe that the steady state case is somewhat more unstable. In particular, for the hybrid case, the calculated critical alpha beta values by the six codes are all above the nominal ITER value of 0.94%, i.e., the hybrid case is stable to the n=19 TAE with alpha particle drive alone. On the other hand, for the steady state case, the results of the three gyrokinetic codes give similar stability thresholds of $\beta_{\alpha,crit} \sim 0.8\%$ which is just below the nominal ITER alpha particle beta value of 1%. Thus the n=19 TAE is found to be weakly unstable with alpha particle drive alone for the steady state case.

Furthermore the results of both GEM and NOVA-K show that beam ions provide a significant destabilization of high-n TAEs with its drive comparable to the alpha particle drive. With both alpha and beam ion drives, the results of GEM simulation indicate that the steady state case is strongly unstable to the high-n TAEs with a broad unstable mode spectrum. The linear growth rate is maximized around n=17.

Initial nonlinear simulations of the n=19 TAE have been carried out for the ITER steady state case using both M3D-K and GEM. The results of M3D-K show that the TAE saturation level scales approximately as the square of linear growth rate for weak instability. This indicates that the wave particle trapping is the dominant saturation mechanism. The GEM nonlinear simulation results show a significant saturation level of the magnetic perturbation around $\delta B_r/B \sim 0.1\%$. Correspondingly the alpha particle density profile is considerably redistributed near the mode peak at r/a~0.6. The redistribution of resonant particles is expected to be larger. We conjecture that multiple unstable alpha-driven TAEs can lead to a significantly larger saturation level and may induce substantial losses of alpha particles and beam ions to the first wall of ITER when coupled to additional loss mechanisms near plasma edge.

3. Specification of ITER parameters and profiles

3.1 TRANSP simulation of ITER profiles: Hybrid case

The TRANSP transport code was used along with GLF23 transport model to predict self-consistently the time evolution within the separatrix. A flat electron density profile was assumed having a Greenwald fraction of 0.85 in the flat-top phase. The impurities were assumed to be helium ash, Be, and Ar. The plasma current was

assumed to be 12 MA. The auxiliary heating was ramped up early to peak D-NNBI, ICRH, and ECH powers of 33, 20, and 20MW; then ramped down to 33, 10, and 7 at 180s. Profiles of the beam heating, momentum input, current drive and fast alpha parameters were calculated using Monte Carlo techniques in the NUBEAM code. The IC heating and current drive profiles are calculated with the TORIC full-wave solver. The EC heating and current drives were calculated with the TORAY code. The resulting q profile is nearly flat in the core of plasma with central value near 1.2. Fig. 3 shows the q profile (upper figure), the normalized alpha particle pressure profile and total pressure profile (lower figure). A fixed boundary was assumed with elongation=1.82, upper triangularity=0.495, lower triangularity=0.295, upper squareness=-0.34, and lower squareness=-0.29. The computed Q_{DT} was 8.8 at the time of the snapshot provided. The main parameters for this hybrid case are: major radius R=6.2m, minor radius a=2m, toroidal magnetic field B_0=5.3T, electron density $n_e(0)=1.05\times10^{20}$ m^{-3}, electron and ion temperature T(0)=25kev, total beta at magnetic axis $\beta(0)$=7.83%, alpha particle beta $\beta_\alpha(0)$=0.94%. Examples of results from similar TRANSP predictions of ITER H and L-mode plasmas are in [Budny12]. Examples of results from TRANSP predictions from a similar ITER Hybrid run are in [Budny13].

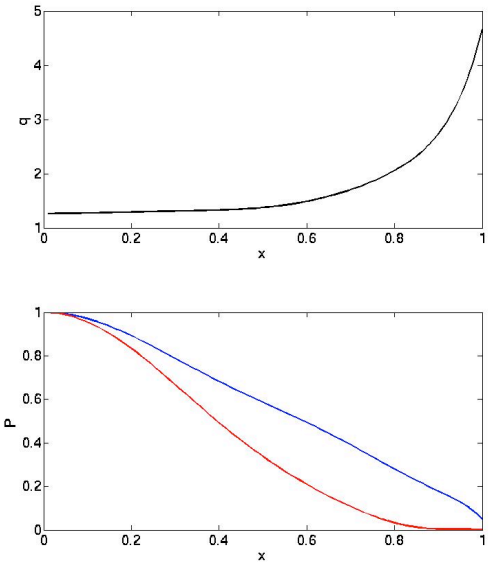

Fig. 3: TRANSP simulated ITER profiles for the hybrid case: (a) safety factor q as a function of x with x being the square root of the normalized poloidal flux; (b) the normalized alpha particle pressure profile (red) and total pressure profile (blue).

3.2 TRANSP/TSC Simulation of the ITER profiles: the steady state case

The time dependent simulations used the free boundary TSC code to evolve the equilibrium and the kinetic profiles and the TRANSP code to calculate the heating and current drive sources. The heating mix used is 33MW of negative ion Neutral Beam distributed on two beam lines, 20MW each of Electron Cyclotron and of Lower

Hybrid. The alpha particle model is a Monte Carlo calculation in TRANSP and Bosch Hale reactivity in TSC. These simulations use a modified Coppi-Tang transport model, with a term to imitate an Internal Transport Barrier in the thermal diffusivity profile. The internal barrier foot is evolved consistently with the location of the minimum in the safety factor profile, consistent with experimental observations with dominant electron heating. The edge barrier is modeled by dropping the thermal diffusivity at the edge to form a pedestal, whose height and width are constrained by peeling-ballooning calculations from EPED1. The plasma operates at a density of 7.0E19, which corresponds to 80% of the Greenwald limit, and has central temperature of about 35keV. Elongation and triangularity are 1.84 and 0.45 respectively. The relaxed solution attains 100% non-inductive current of 9MA, β_N=2.7 and fusion gain of Q=5 and the equilibrium is ideal MHD stable [Poli12]. More recent simulations using the CDBM transport model to trigger and evolve the internal barriers converge to steady-state solutions in the same range of parameters [Poli14]. Fig. 4 gives the q profile (upper figure) and the normalized alpha particle pressure, total pressure and electron density profiles (lower figure). The main parameters for this steady state case are: major radius R=6.2m, minor radius a=2m, toroidal magnetic field B_0=5.3T, electron density $n_e(0)=7.0\times10^{19}$ m^{-3}, electron and ion temperature T(0)=36.2kev, total beta at magnetic axis β(0)=7.96%, alpha particle beta $\beta_\alpha(0)$=1.0%.

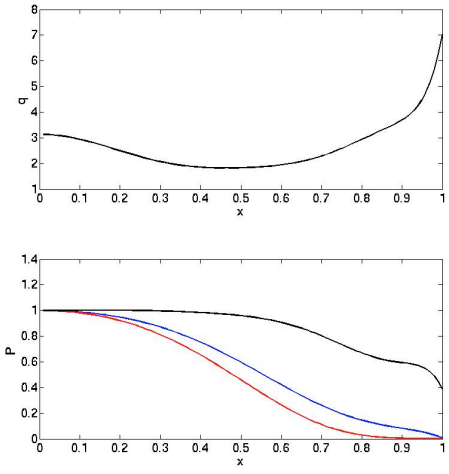

Fig. 4. TRANSP/TSC simulated ITER profiles for the steady state case: (a) safety factor q as a function of x with x being the square root of the normalized poloidal flux; (b) the normalized alpha particle pressure profile (red), total pressure profile (blue) and electron density profile (black).

4. Linear Simulations

4.1 NOVA/NOVA-K

In this joint work we use NOVA/NOVA-K codes to calculate the stability of TAEs for the ITER hybrid case and the steady state case.

NOVA is a suite of codes that are based on the ideal MHD solver for perturbative and non-perturbative eigenmodes. Widely used version of the code solves for perturbative modes as well as for the Alfvenic/acoustic continuum which was originally published in Ref. [Cheng86]. A kinetic extension to NOVA, known as NOVA-K, was subsequently written over years and began in Ref. [Cheng92]. We mention here several key papers that are often used to study the stability properties of TAE modes. The trapped electron collisional damping is implemented according to Ref. [Fu93]. Drift kinetic formulation including finite orbit width (FOW) effects can be found in Ref. [Gorelenkov99]. In that reference an important result was confirmed numerically that FOW leads to a plateau in the growth rate dependence on the toroidal mode number which limits the number of unstable modes in ITER for example. The advantage of using NOVA/NOVA-K codes is its relatively fast computations of AE stability properties and in its package of various damping and driving kinetic effects included in the simulations. The NOVA codes are widely used to study the linear stability properties of Alfvenic modes and have been extensively verified and validated [Zeeland06, Kramer06]. In particular, the NOVA codes have been applied to investigate the stability of alpha-driven TAEs in ITER [Gorelenkov03, Gorelenkov05]. In this work the stability of alpha-driven TAEs is calculated perturbatively based on the ideal MHD solutions of TAEs.

Hybrid ITER plasma

n=15 AE stability at $\beta_\alpha = 4\%$

We set up the equilibrium profiles for the ITER hybrid case, having nearly zero magnetic shear region near the center where we have found the so-called core-localized TAEs. First we show on the left in Fig. 5 the Alfvén continuum structure where the acoustic continuum effect is accounted for by up-shifting the shear Alfvén continuum by the GAM frequency at the specific heat ratio $\gamma = 1.3$.

For this case and the same toroidal mode numbers we computed localized TAE solutions. They are shown on right in Fig. 5 depicting the radial component of the displacement vector multiplied by $\nabla\psi$. The solutions are chosen from the two most unstable modes calculations at $n = 15$. These MHD solutions are localized around strong gradient regions of beam and alpha pressures. Table 3 lists the alpha particle drive, the electron collisional damping rate, the ion Landau damping, the radiative

damping, the poloidal mode number for the largest harmonic, and the critical on-axis alpha beta value.

The results of n=19 and n=23 are shown in Fig. 6/Table 4 and Fig. 7/Table 5 respectively.

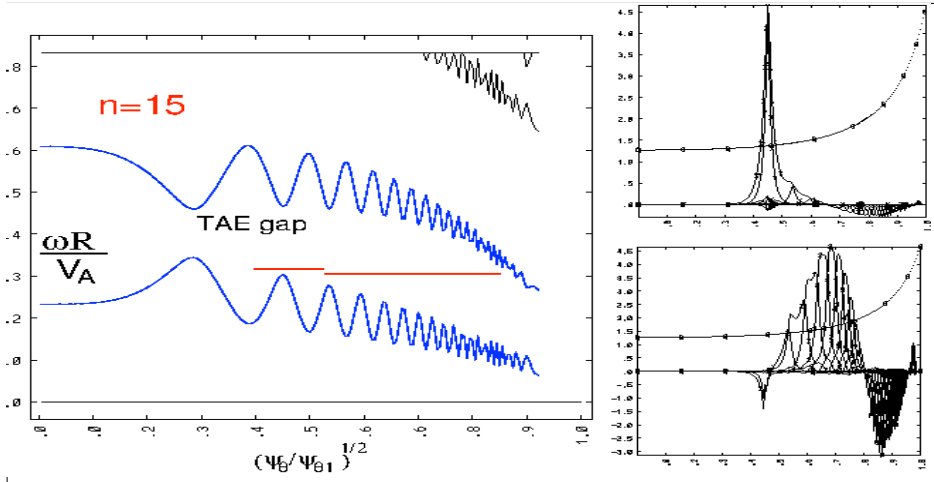

Fig.5. Alfvén continuum around the TAE frequency profile for ITER hybrid scenario plasma is shown on the left figure for $n = 15$. Solid red lines show the location and the frequency of TAE modes found for this case. Right figures depict the radial displacement poloidal harmonics of these modes that are most unstable.

Table 3: All growth rates are in % and are obtained at the prescribed value of alpha beta $\beta_{\alpha 0} = 4\%$.

ω/ω_A	γ_α/ω	γ_{eColl}/ω	$\gamma_{iLandau}/\omega$	γ_{radiat}/ω	m_{max}	$\beta_{\alpha 0crit}$, %
0.302	8.09	-0.07	-0.4	-2.9	26	1.66
0.308	6.85	-0.11	-2.55	-2.26	21	2.87

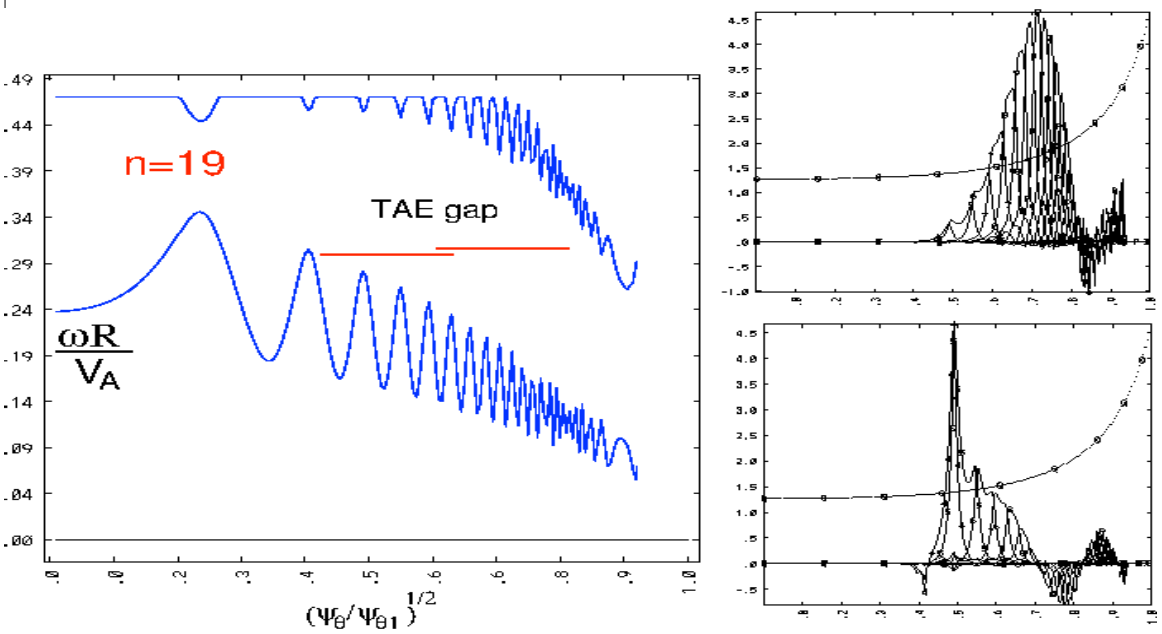

Fig.6. Alfvén continuum around the TAE frequency profile for ITER hybrid scenario plasma is shown on the left figure for $n = 19$*. Right figures depict the radial displacement poloidal harmonics of these modes that are most unstable.*

Table 4: All growth rates are in % and are obtained at $\beta_{\alpha 0} = 4\%$.

ω/ω_A	γ_α/ω	γ_{eColl}/ω	$\gamma_{iLandau}/\omega$	γ_{radiat}/ω	m_{max}	$\beta_{acrit}, \%$
0.3	7.06	-0.11	-1.2	-4.1	26	3.07
0.31	6.07	-0.06	-0.14	-3.65	47	2.54

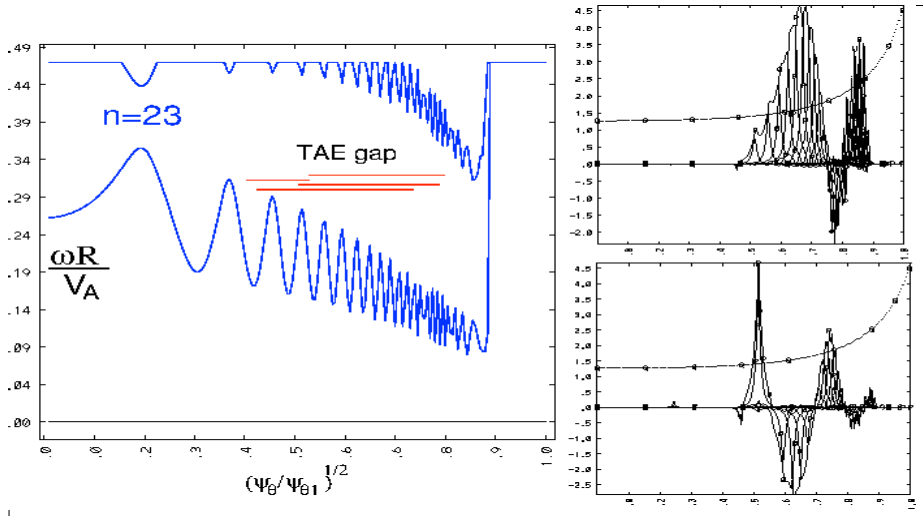

Fig.7. Alfvén continuum around the TAE frequency profile for ITER hybrid scenario plasma is shown on the left figure for $n = 23$. Right figures depict the radial displacement poloidal harmonics of these modes that are most unstable.

Table 5: All growth rates are in %

ω/ω_A	γ_α/ω	γ_{eColl}/ω	$\gamma_{iLandau}/\omega$	γ_{radiat}/ω	m_{max}	$\beta_{\alpha 0crit}$, %
0.295	3.99	-0.12	-0.53	-5.59	32	Stable
0.3036	3.68	-0.08	-0.13	-6.12	37	Stable

Steady state case

n=15 AE stability analysis at $\beta_\alpha = 2.64\%$

A similar analysis was done for the ITER steady state case and the results of n=15 are summarized in Fig. 8. We did not find a localized RSAE solution in the TAE gap, that is normally expected for the reversed shear plasma. However several TAE modes were computed by NOVA and analyzed for stability with NOVA-K code. The results are summarized in the Table 6.

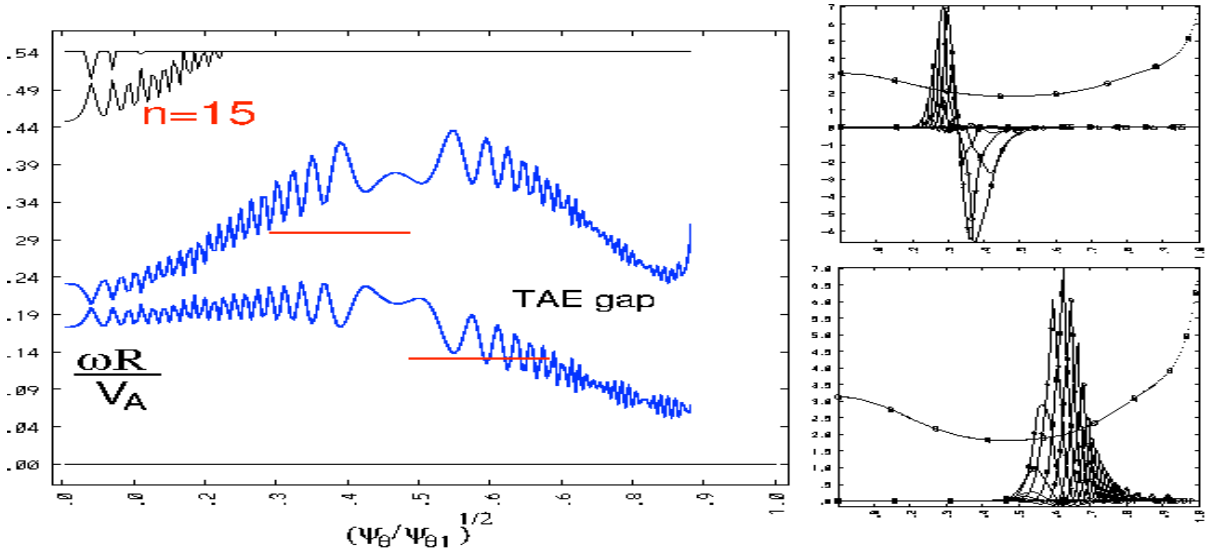

Fig.8. Alfvén continuum for RS ITER plasma showing several gaps on the left figure with the locations and frequencies of three representative modes, BAE and TAE. Figures with the mode structures are presented on the right and include the safety factor profiles with clear reversed shear region at around $\sqrt{\psi_0} \simeq 0.45$.

Table 6: All growth rates are in % and are obtained at the prescribed alpha and beam beta value of $\beta_{\alpha 0} = 2.64\%$, $\beta_{NBI0} = 0.71\%$.

ω/ω_A	γ_α/ω	γ_{NBI}/ω	γ_{eColl}/ω	$\gamma_{iLandau}/\omega$	γ_{radiat}/ω	m_{max}
0.139	49	22.6	-0.22	2.3	no results	31
0.299	3.16	1.49	-0.1	0.3	-3.63	29

n=19 AE stability analysis at $\beta_\alpha = 2.64\%$

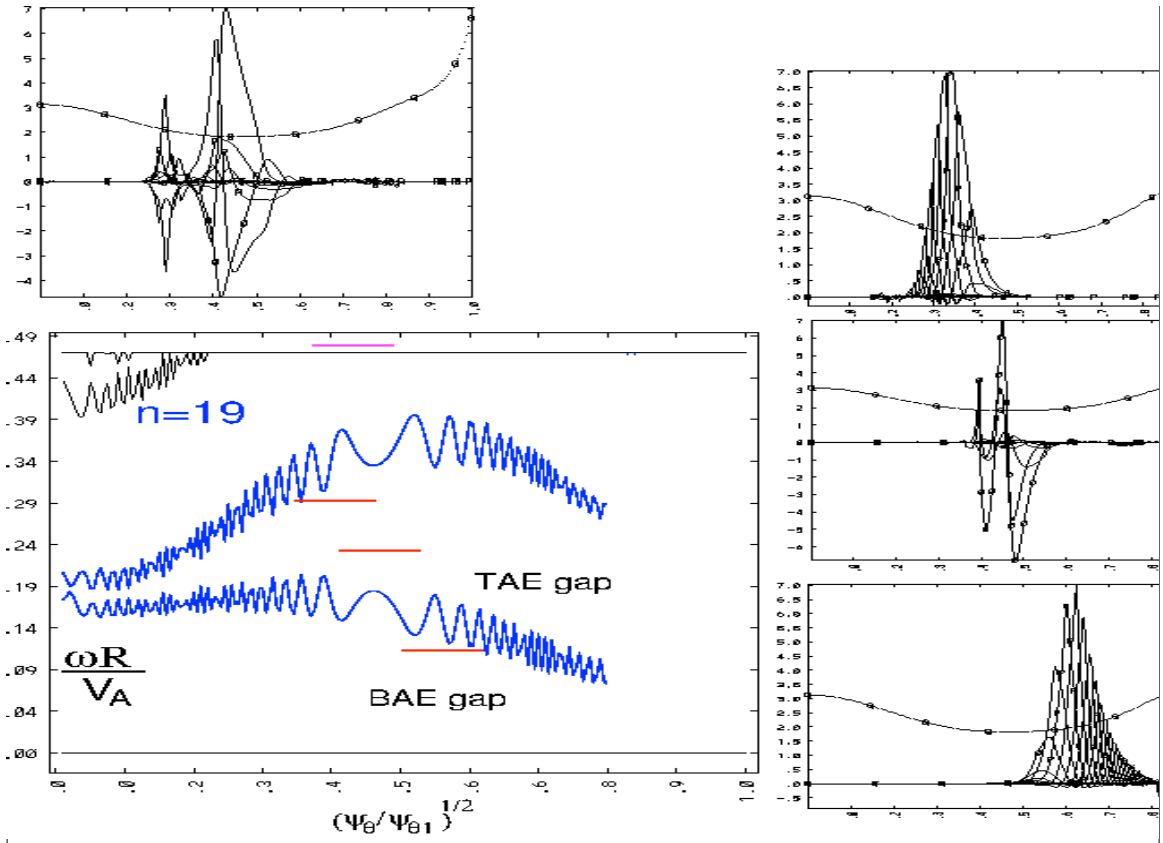

Fig.9. Alfvén continuum for RS ITER plasma showing TAE gap. Figures with the most unstable mode structures are presented on the right and include the safety factor profiles with clear reversed shear region at around $\sqrt{\psi_0} < 0.45$.

Table 7: All growth rates are in % and are obtained at the prescribed value of alpha and beam beta $\beta_{\alpha 0} = 2.64\%$, $\beta_{NBI0} = 0.71\%$. Beta critical of alphas is again computed with fixed beam ion drive.

ω/ω_A	γ_α/ω	γ_{NBI}/ω	γ_{eColl}/ω	$\gamma_{iLandau}/\omega$	γ_{radiat}/ω	m_{max}	$\beta_{\alpha 0crit}$, %
0.31	0.16	0.17	-0.11	-3.6	-4.09	37	stable
0.224	2.14	1.1	-0.13	0.67	-3.04	34	1.73
0.138	6.16	8.5	-0.21	-	-	38	no results

4.2 TAEFL

The TAEFL model [Spong92, Spong94] uses optimized gyro-Landau fluid closures [Spong13] to incorporate energetic particle wave – particle resonance effects into a reduced MHD model. This model has been verified [Spong12] against other gyrokinetic models and validated with data from DIII-D for an n = 3 upsweeping frequency RSAE instability. It has also recently been applied [Spong14] to the nonlinear regime of coupled RSAE/TAE instabilities. Ion and electron Landau damping terms are included and coupling to the kinetic Alfvén wave is retained based on an expansion of the thermal ion FLR term. This model has been applied both to the ITER hybrid and steady-state scenario cases.

Hybrid Regime Case - For the hybrid case 400 radial grid points and 30 poloidal mode numbers were used. The distribution of poloidal mode numbers was selected so as to be centered about where the mode structure peaked. For example, at *n =10,* modes *m = 1* to *30* were used, while for *n =23,* modes *m = 11* to *40* were used. In Figure 10 typical results for the hybrid scenario (monotonic q-profile) are plotted for the linear growth rate and real frequency variation with the toroidal mode number for *n = 10* to *n = 23.* The regular frequency and growth rate variations are correlated with the most unstable mode moving around in radius and within the main TAE frequency gap as the toroidal mode number is changed. The *n's* with the higher frequencies (i.e., *n = 14, 17, 20*) are typically dominated by two coupled poloidal mode numbers and localized around *r/a ~ 0.3*. The *n's* with the higher frequencies (i.e., *n = 12, 15, 18*) are typically dominated by a broader range of coupled poloidal modes and localized around *r/a ~ 0.4*.

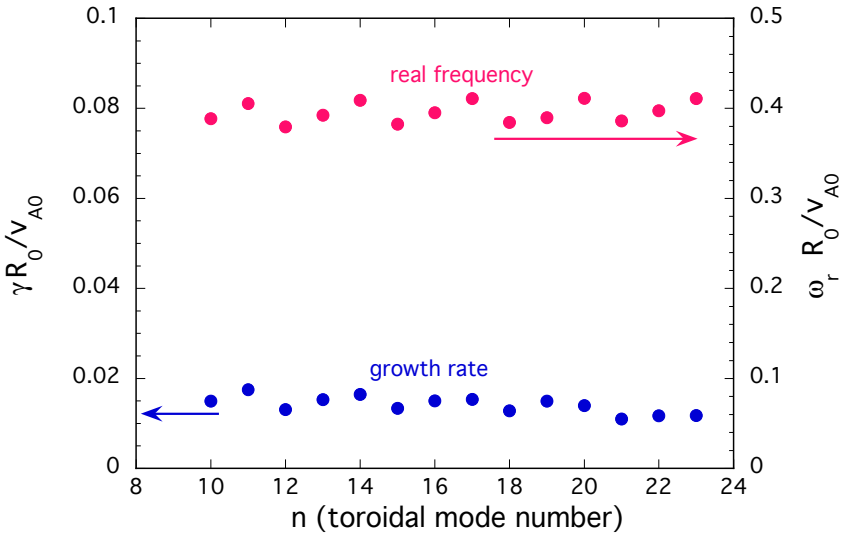

Fig. 10: Growth rates and real frequencies vs. toroidal mode number (n) at $\beta_\alpha(0) = 0.04$ for the hybrid regime case.

In Figure 11, a scan of the growth rate and frequency is give vs. the central alpha particle β value for *n = 15* and *n = 19*. Based on extrapolations back to zero growth rate, the marginal stability threshold in $\beta_\alpha(0)$ falls between ~ *1.98%* and *2.12%*, well above the predicted $\beta_\alpha(0) = 0.94\%$ given by the TRANSP simulation for this case.

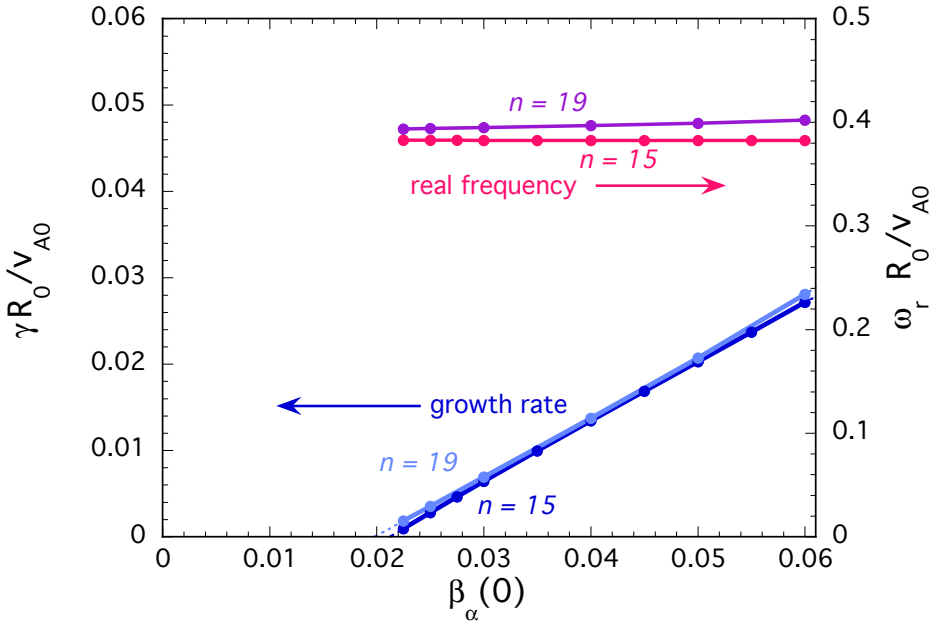

Figure 11 – Growth rates and real frequencies of n=15 and n=19 versus on axis alpha beta $\beta_\alpha(0)$ for the hybrid regime case.

The mode structure variation with toroidal mode number is plotted in Figure 12. The 2D mode structure contours and radial eigenfunctions of the potential function at $\beta_\alpha(0) = 0.04$ are displayed for *n = 15* (higher real frequency), *n = 19* (lower real frequency) and *n = 23* (lower real frequency). The radial eigenfunction plots also show the *q-profile* and indicate the dominant mode pair *(m,n)* at the top of the plot. A similar variation in mode structure and localization is also found in comparing the *n = 11, 12* and *17, 18* cases. The *n = 10, 13, 16* cases are more similar to the lower frequency cases of Figure 12 while the *n = 19, and 20* modes are closer in structure to the higher frequency case of Figure 12.

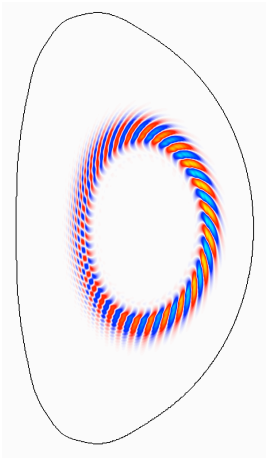

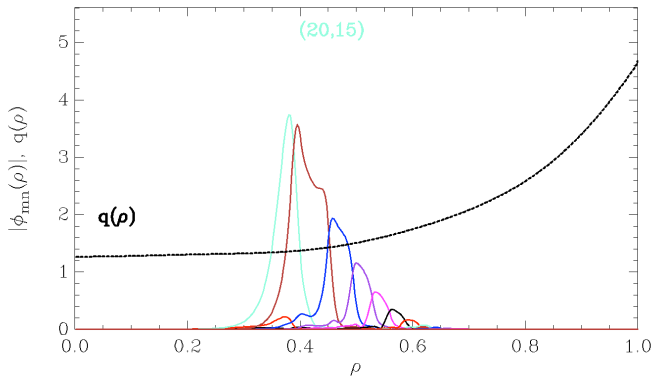

n = 15

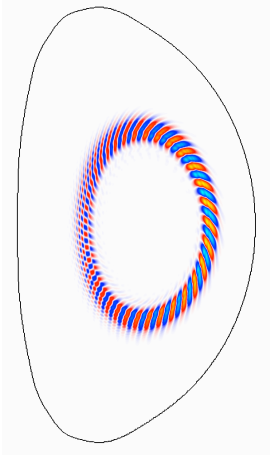

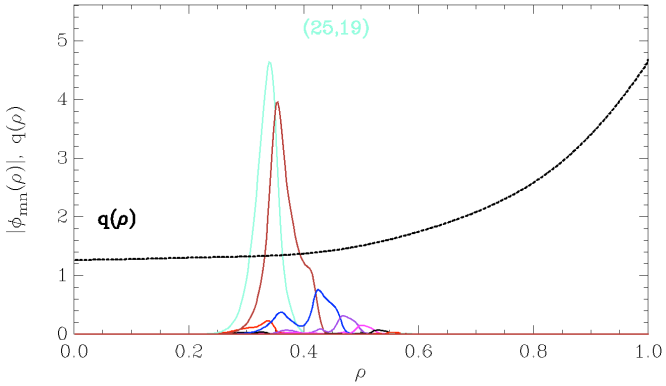

n = 19

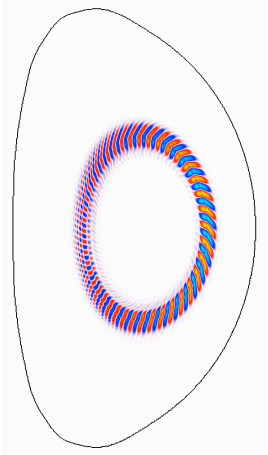

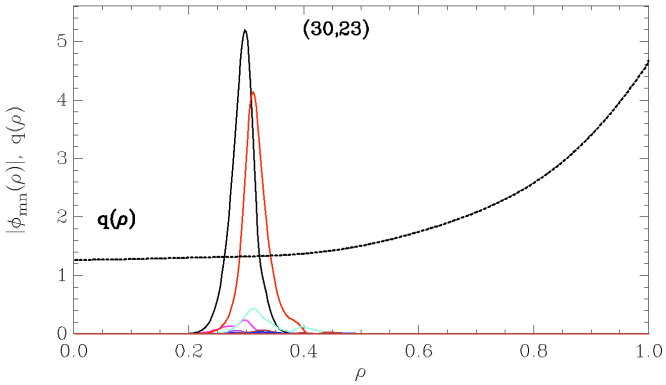

n = 23

Figure 12 – 2D (left column) and radial eigenmode (right column) structures for the hybrid case n = 15, 19, and 23 at $\beta_\alpha(0) = 0.04$.

Steady-State Regime Case - The TAEFL model has also been applied to the steady-state scenario case. This differs from the hybrid scenario in that the *q-profile* is non-monotonic. It has a minimum of $q \sim 1.8$ near $\rho = (\psi_{tor}/\psi_{tor,edge})^{1/2} = 0.5$. For these calculations, 400 radial points and 30 poloidal modes ($m_{min} = 4 - 12$, $m_{max} = 33 - 41$, depending on the n value) again were used. Figure 13 plots the growth rates and real frequencies vs. *n*. Peaks in the growth rate are present at $n = 13$ and a lower peak at $n = 18$. The frequencies ($\omega R_0/v_{A0} \sim 0.25$) are lower than was the case for the hybrid case ($\omega R_0/v_{A0} \sim 0.4$).

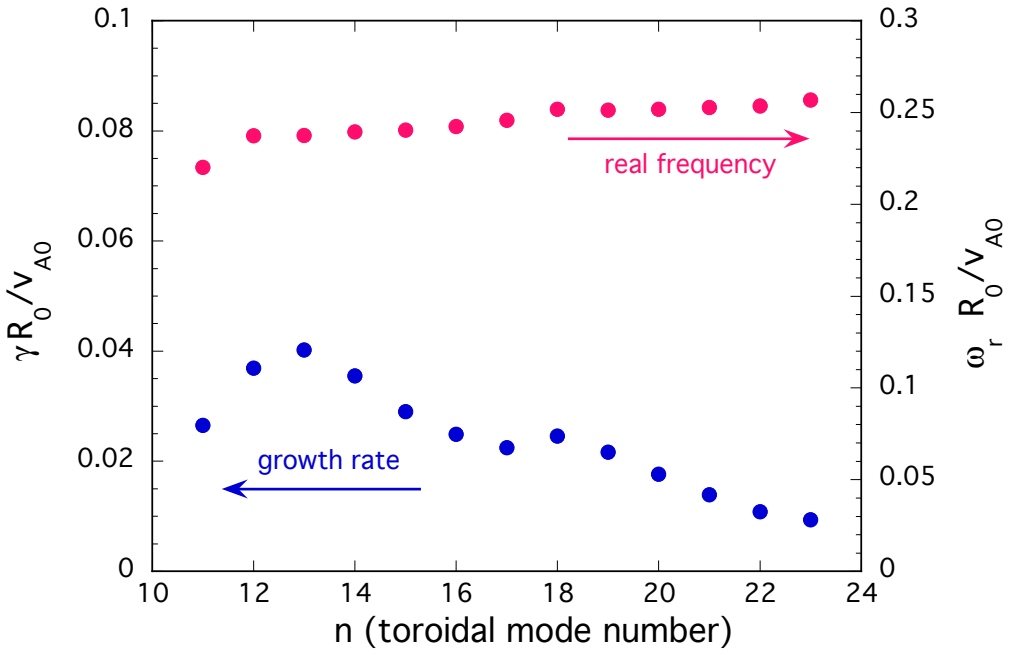

Figure 13 – Growth rates and real frequencies vs. toroidal mode number (n) at $\beta_\alpha(0) = 0.0264$ for the steady-state regime case.

The $\beta_\alpha(0)$ scan is given in Figure 14 is for $n = 15$ and 19. This indicates that extrapolated growth rates remain finite below $\beta_\alpha(0) = 0.01$, with an extrapolated threshold near $\beta_\alpha(0) = 0.005$ for $n = 15$ and $\beta_\alpha(0) = 0.0075$ for $n = 19$; the TRANSP predicted $\beta_\alpha(0)$ for this case is 0.0102.

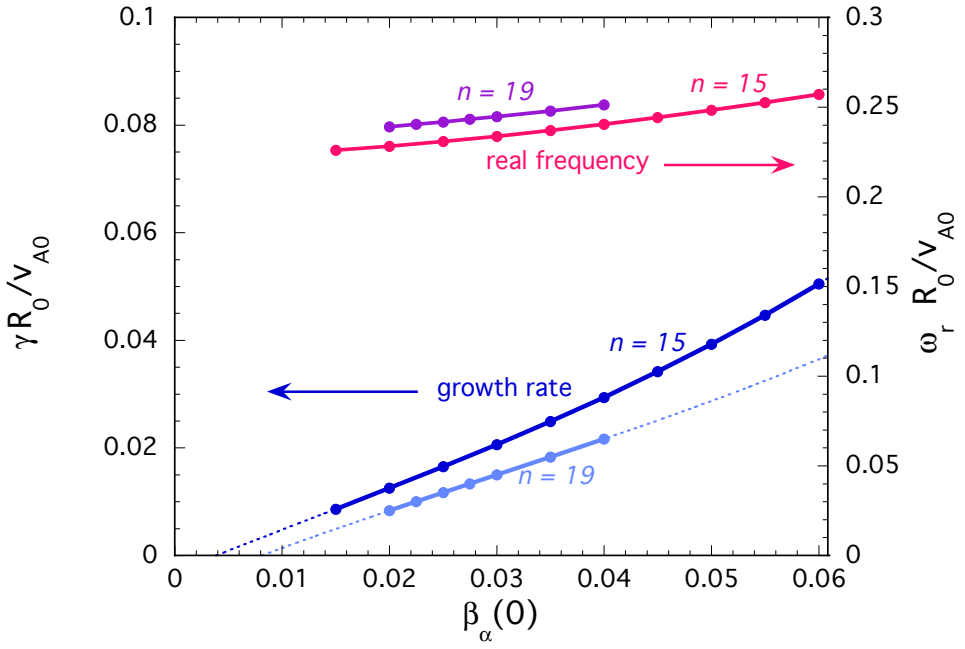

Figure 14 – Growth rates and real frequencies vs. $\beta_\alpha(0)$ for n = 15, and 19 for the steady-state regime case.

Some of the mode structures are plotted in Figure 15, showing that the modes typically involve coupling over a range of poloidal modes and are localized near or slightly outside the minimum in the *q-profile*.

Summary – The TAEFL gyro-Landau closure model has been applied to Alfvén instabilities in ITER for both hybrid regime and steady-state regime cases. Good convergence in the calculations was obtained by using 400 flux surfaces and 30 poloidal modes, with the range of the poloidal modes shifted as the toroidal mode number is changed in order to provide good coverage around the dominant poloidal mode. Cases were checked with larger numbers of poloidal modes and flux surfaces (up to 800) with little change in the results. Of the two regimes, the steady-state case has the lowest stability thresholds. Based on TRANSP predictions of the expected $\beta_\alpha(0)$, the Alfvén instabilities analyzed here should be readily observable in the steady-state regime, but stable in the hybrid regime. Nonlinear runs for the steady-state regime are also underway with this model to determine the nonlinear dynamics and saturation level.

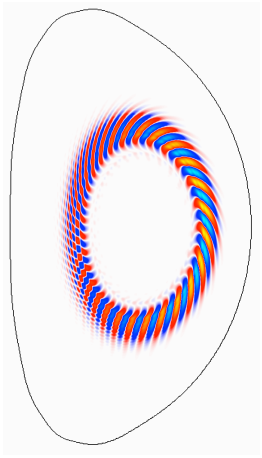

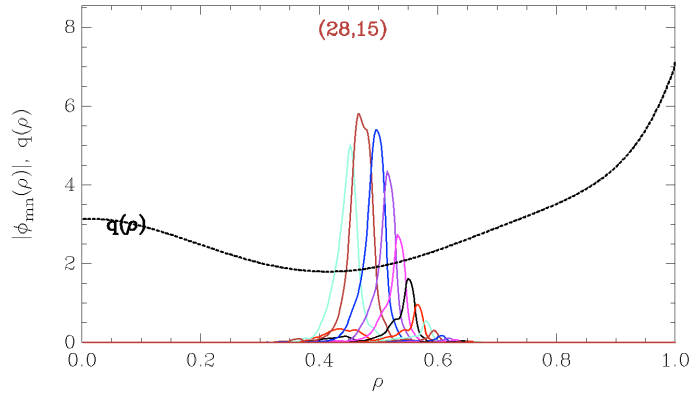

n = 15

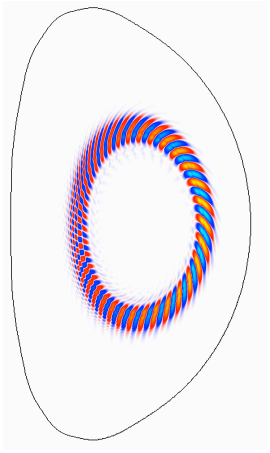

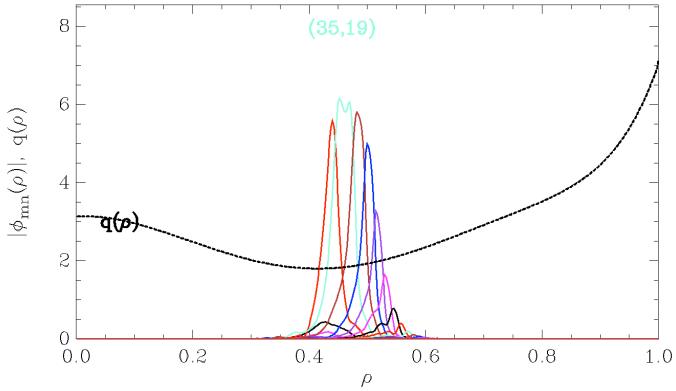

n = 19

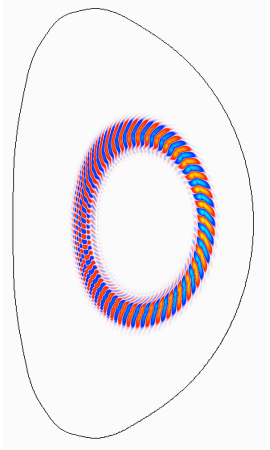

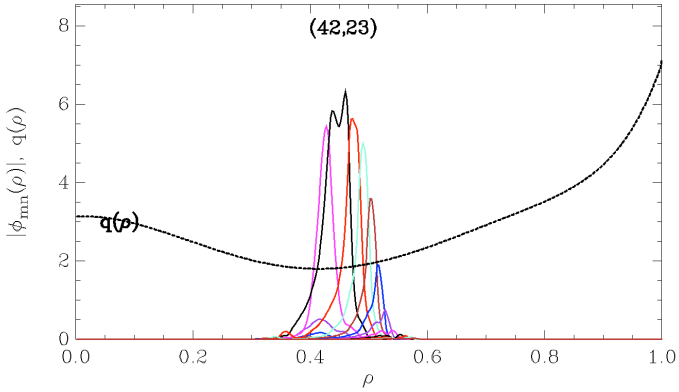

n = 23

Figure 15 – 2D and radial eigenmode structures for n = 15, 19, and 23 for steady-state case at $\beta_\alpha(0) = 0.0264$

4.3 M3D-K

For this joint work, a beta alpha scan of the n=19 TAE was performed for the ITER hybrid case and the steady state case using the kinetic-MHD hybrid simulation code M3D-K [Fu06]. In the hybrid model, the thermal plasmas are treated as single fluid and the energetic particles are described using the drift-kinetic equation. The effects of energetic particles enter in the model in the momentum equation via the stress tensor term. The code uses general equilibria with finite beta, finite aspect ratio, and arbitrary plasma shape. The code has recently applied to investigate nonlinear evolution of energetic particle-driven TAEs with effects of energetic particle collision, particle source and sink [Lang10], as well as effects of plasma micro-turbulence [Lang11]. The code has also been applied to simulate beam-driven TAEs in NSTX [Liu13] and beam-driven RSAE in DIII-D [Fu12]. In this work, the effects of collisions are neglected. It should be noted that the M3D-K model used in this work includes alpha particle drive as well as continuum damping and viscous damping. The ion Landau damping and the radiative damping are not included.

Hybrid case

Figure 16 shows the hybrid scenario n=19 growth rate for different values of the on axis alpha beta. When alpha beta is adjusted, the TAE frequency remains approximately constant near ω/ω_A=0.031. The n=19 TAE has an alpha beta threshold of approximately $\beta_{\alpha 0}$=3.5%. The n=19 TAE mode structure is shown in Fig. 17 for 2D contour on a poloidal plane (left) and for poloidal harmonics as a function of radius (right).

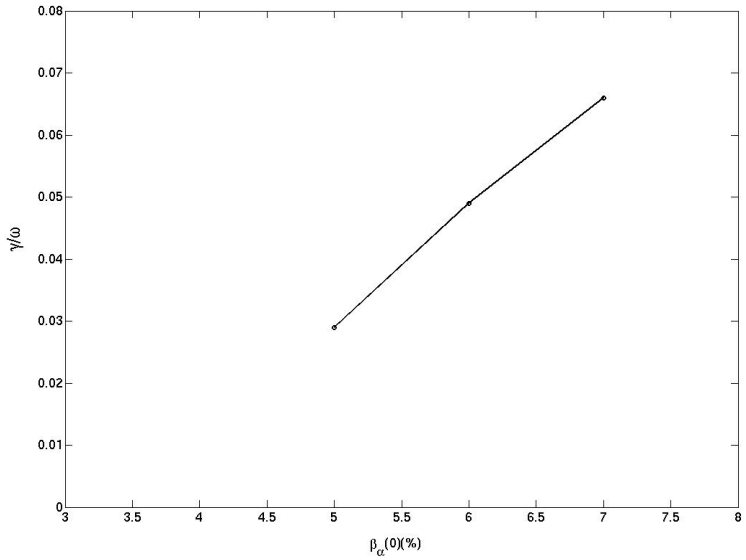

Figure 16: TAE growth rate for the hybrid equilibrium is plotted vs. the on axis alpha beta.

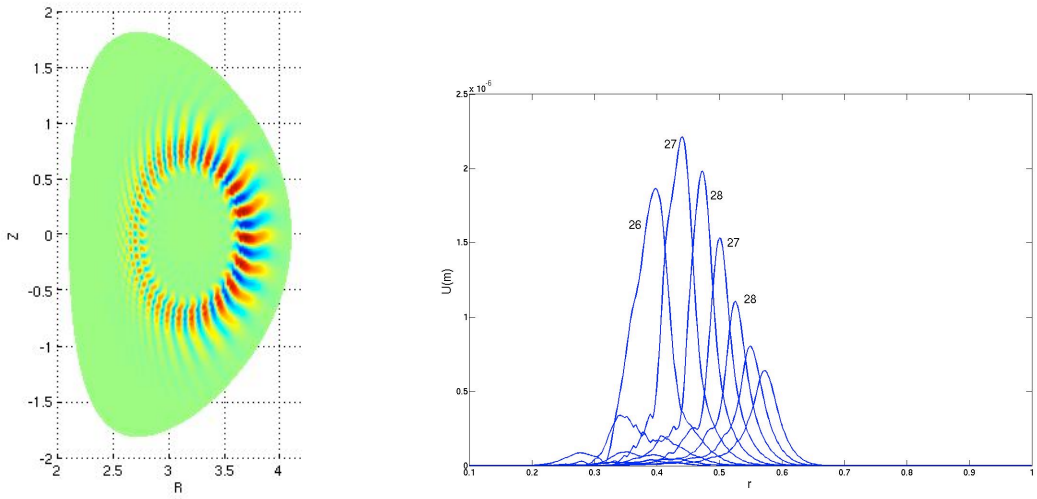

Figure 17: Contour of velocity stream function U plotted on a poloidal cross section for the n=19 TAE of the ITER hybrid case.

Steady state equilibrium

Figure 18 shows the steady state n=19 TAE growth rate for different values of the on axis alpha beta. The growth rate has an on axis alpha beta threshold of $\beta_{\alpha 0}$=1.0%. The n=19 TAE mode structure is shown in Fig. 19 for 2D contour on a poloidal plane (left) and for poloidal harmonics as a function of radius (right).

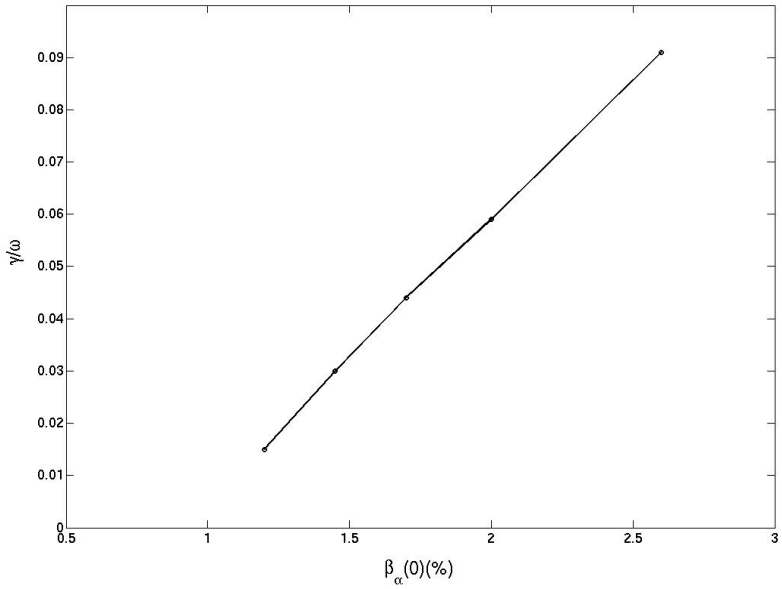

Figure 18: TAE growth rate is plotted vs. central alpha beta $\beta_{\alpha 0}$

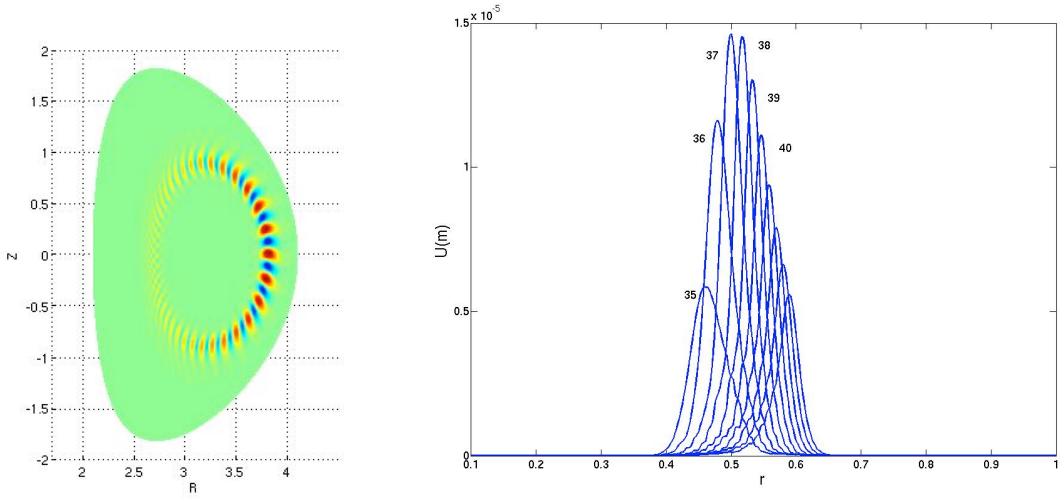

Figure 19: Plasma velocity stream function U plotted in a poloidal cross-section (left) and versus radius for poloidal harmonics from m=35 to m=44 (right).

4.4 GEM

The Gyrokinetic delta-f PIC code GEM is used in this study. The Miller parameterization of a flux surface shape is used to model a general magnetic equilibrium [Chen07]. Both the thermal ions and the energetic particles are gyrokinetic, but the electrons are described with a fluid model, consisting of the electron continuity equation and the parallel Ohm's law. The electron inertia effect is neglected in the Ohm's law. The electron temperature is assumed to be constant along the perturbed magnetic field line, which provides a closure relation for the electron pressure that appears in the continuity equation and the Ohm's law. The vorticity equation is used to obtain the electric potential, instead of the usual gyrokinetic Poisson equation [Chen13]. The alpha particle distribution is the slowing-down distribution. For each equilibrium, a scan over the toroidal mode number is first performed at a fixed alpha beta value to determine the most unstable mode. Then for n=19, a scan over the alpha beta is performed to determine the stability threshold. The magnetic equilibrium is held fixed as the alpha or beam particle beta varies.

Hybrid case

Results are shown in Figures 20-24. Figure 20 shows n-scan results for the hybrid case at β_α=4%. The most unstable mode is n~16, with the growth rate roughly constant for 15<n<20. These linear simulations use a grid resolution of (nx,ny,nz)=(256,32,32) in the field-aligned coordinates, 8 particles per spatial cell per species. For all other simulations the radial grid number is 512. Figure 21 shows beta-scan for n=19 mode. Extrapolating the mode growth rate to zero, an alpha beta threshold of 2.2% is obtained. These linear simulations use a grid resolution of (nx,ny,nz)=(512,32,64) in the field-aligned coordinates, 8 particles per cell per ion

species. Figure 22 shows the 2D contour (left) and radial functions of poloidal harmonics (right) for the n=15 electric potential for the hybrid case at β_{α}=4%. The simulation domain used is [0.1,1] in r/a. The complex mode frequency is ω/ω_A = (0.31, 0.037). The results of n=19 and n=23 are shown in Fig. 23 and Fig. 24 respectively.

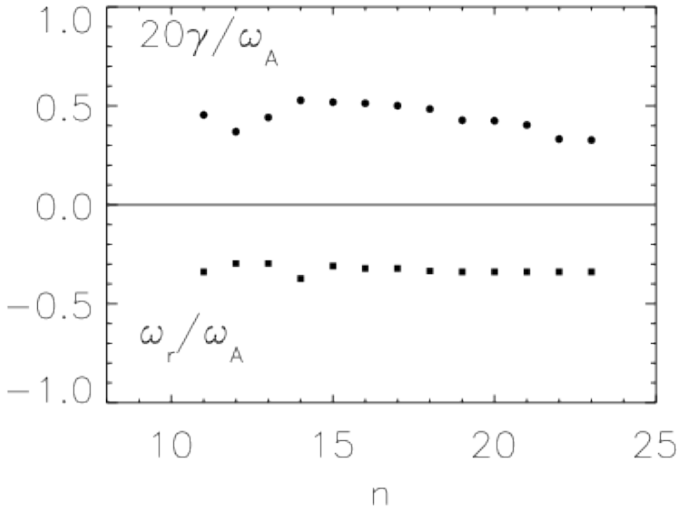

Figure 20: Growth rate and mode frequency versus toroidal mode at β_{α}=4%.

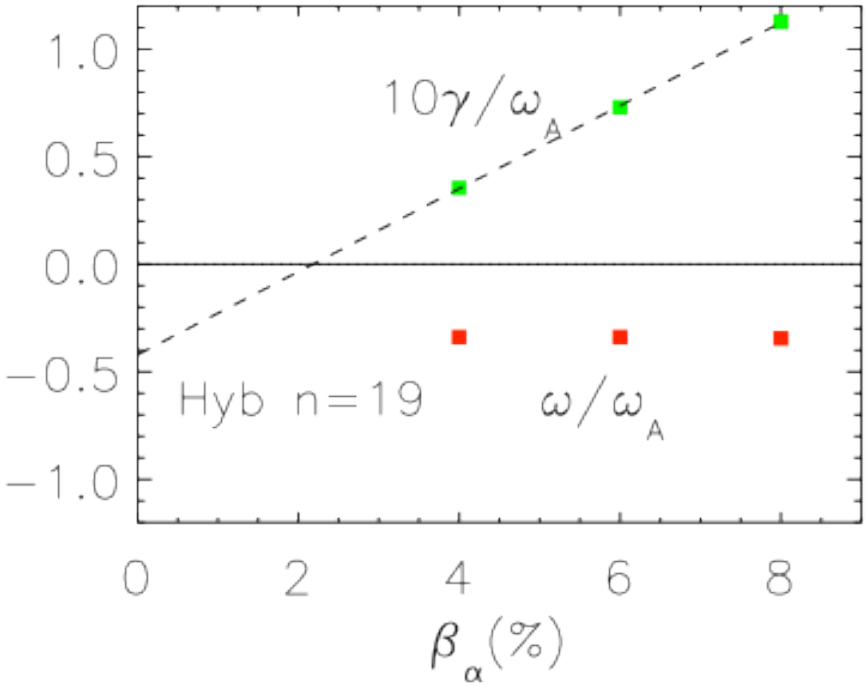

Figure 21: beta-scan for n=19 for Hybrid equilibrium.

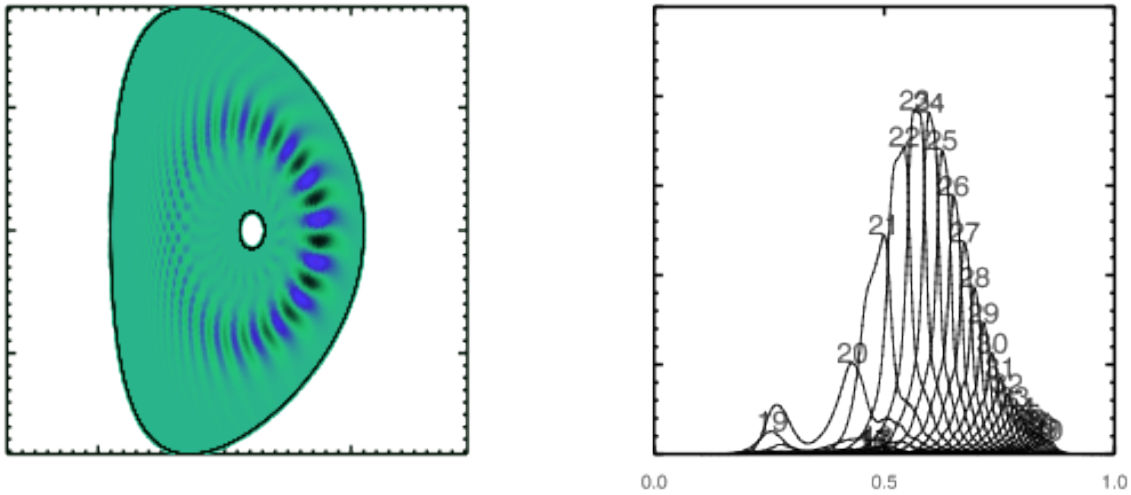

Figure 22: 2D contour (left) and poloidal harmonics versus radius (right) of n=15 electric potential for the hybrid case at β_α=4%. The simulation domain is r/a in [0.1, 1]. The complex mode frequency is ω/ω_A = (0.31, 0.037)

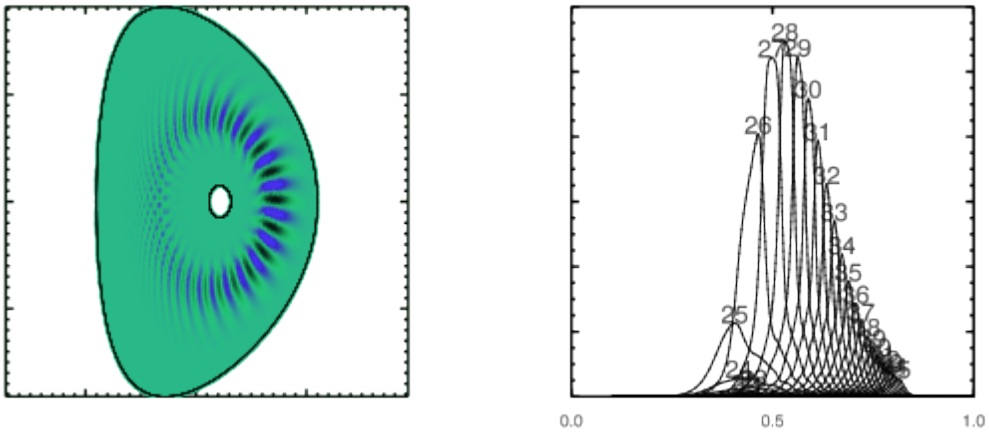

Figure 23: 2D contour (left) and poloidal harmonics versus radius (right) of n=19 electric potential for the hybrid case at β_α=4%. The complex mode frequency is ω/ω_A = (0.34, 0.036)

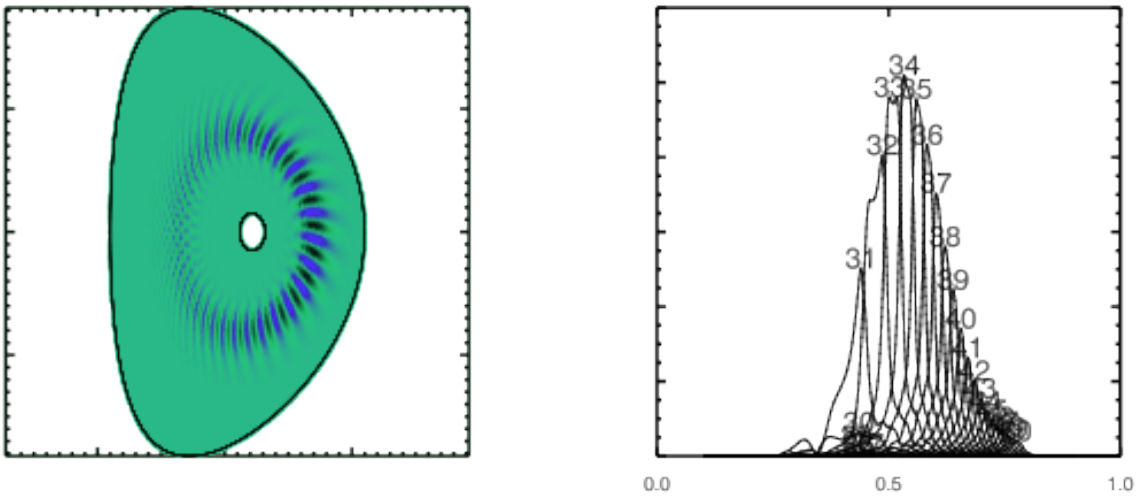

Figure 24: 2D contour (left) and poloidal harmonics versus radius (right) of n=23 electric potential for the hybrid case at β_α=4%. The complex mode frequency is ω/ω_A = (0.35, 0.027)

Steady state equilibrium

Results of the steady state case are shown in Figures 25-29. Figure 25 shows n-scan results for the steady state case at β_α=2.64%. The most unstable mode is n~17, with the growth rate roughly constant for 11<n<30. Figure 26 shows beta-scan for n=19 mode. Extrapolating the mode growth rate to zero, an alpha beta threshold of 0.7% is obtained. Alpha driven modes become dominant at the nominal alpha pressure β_α=1.0%. This equilibrium has a reversed shear q-profile, but a scan over the minimum q does not show fast sweeping of the mode frequency. Figure 27 shows the 2D contour (left) and radial functions of poloidal harmonics (right) for the n=15 electric potential at β_α=4%. The simulation domain used is [0.1, 0.9] in r/a. The results of n=19 and n=23 are shown in Fig. 28 and Fig. 29 respectively.

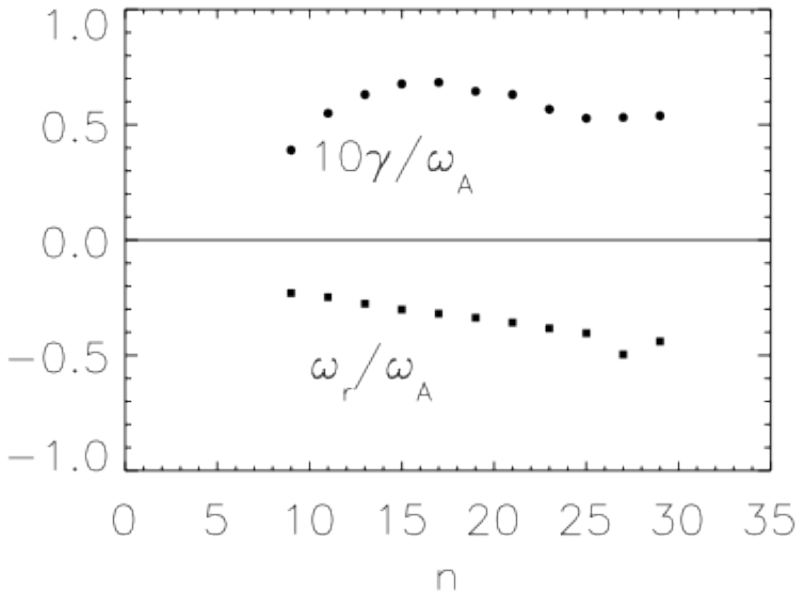

Figure 25: Growth rate and mode frequency versus toroidal mode for the steady state case at β_α=2.64%. The most unstable mode is n~17.

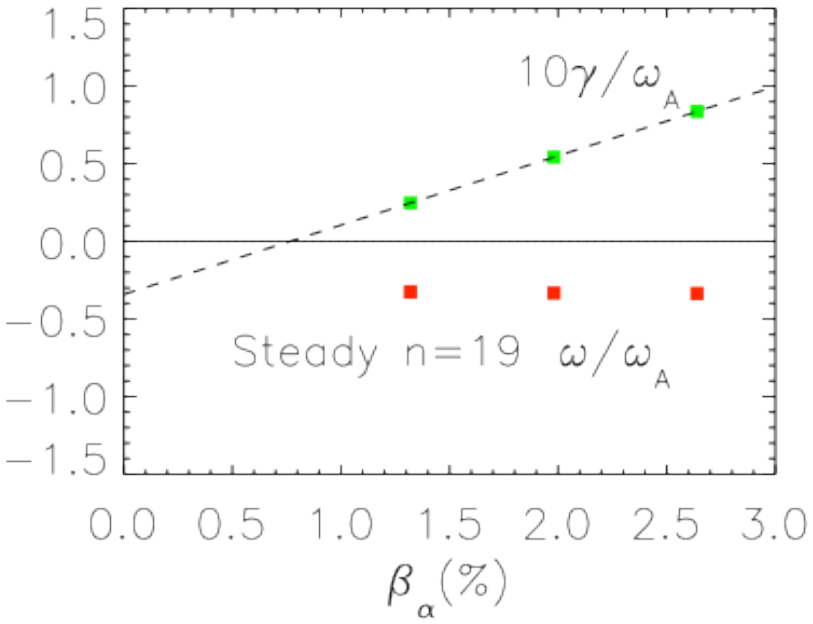

Figure 26: beta-scan for n=19, Steady State equilibrium. As $\beta_\alpha$increases an alpha-driven mode becomes unstable with ω/ω_A=0.3. Extrapolating the mode growth rate to zero, an alpha pressure threshold of β_α~0.7% is obtained.

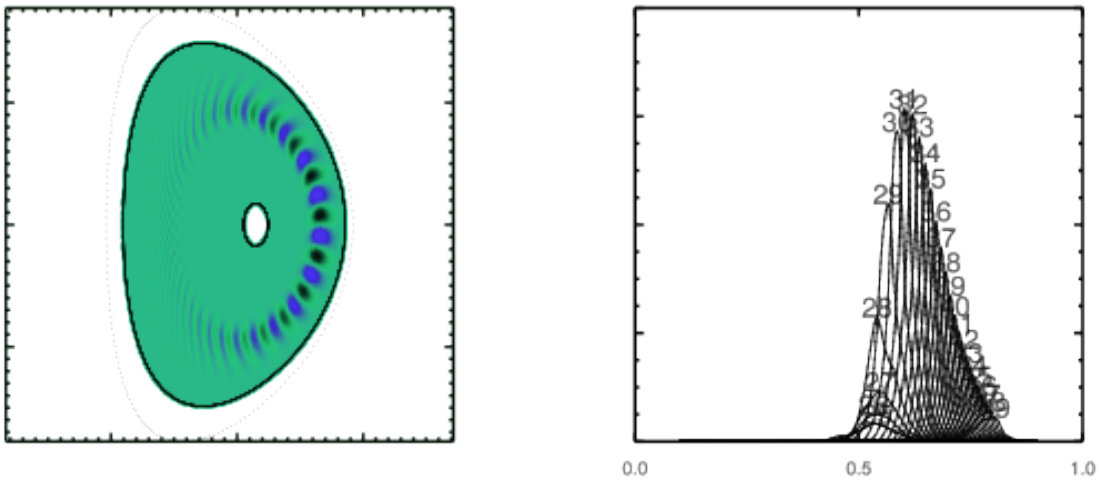

Figure 27: 2D contour (left) and poloidal harmonics versus radius (right) of n=15 electric potential for the steady state case at β_α=2.64%. The simulation domain is r/a in [0.1,0.9]. The last closed surface r/a=1 is shown in dotted line. The complex mode frequency is ω/ω_A = (0.30, 0.085).

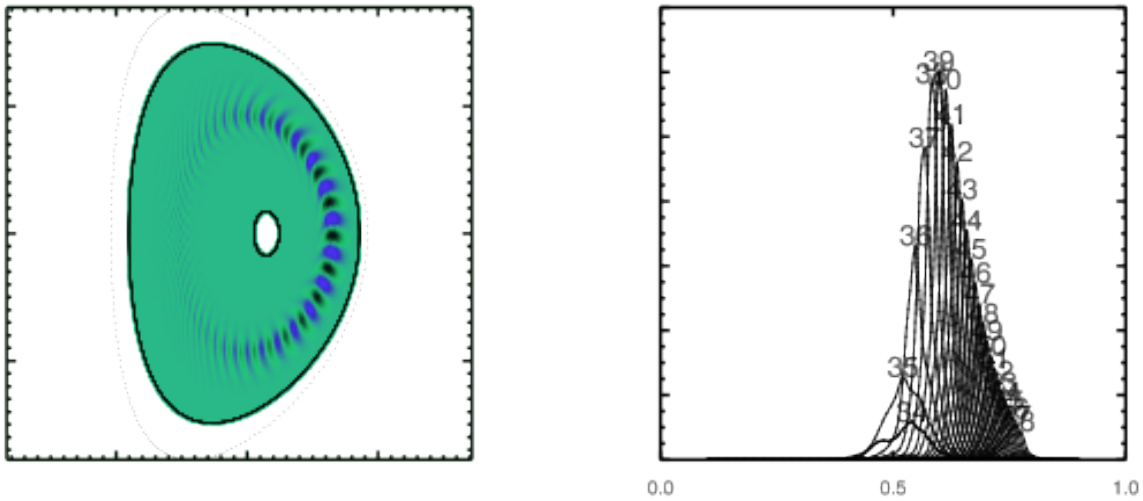

Figure 28: 2D contour (left) and poloidal harmonics versus radius (right) of n=19 electric potential for the steady state case at β_α=2.64%. The complex mode frequency is ω/ω_A = (0.34, 0.084)

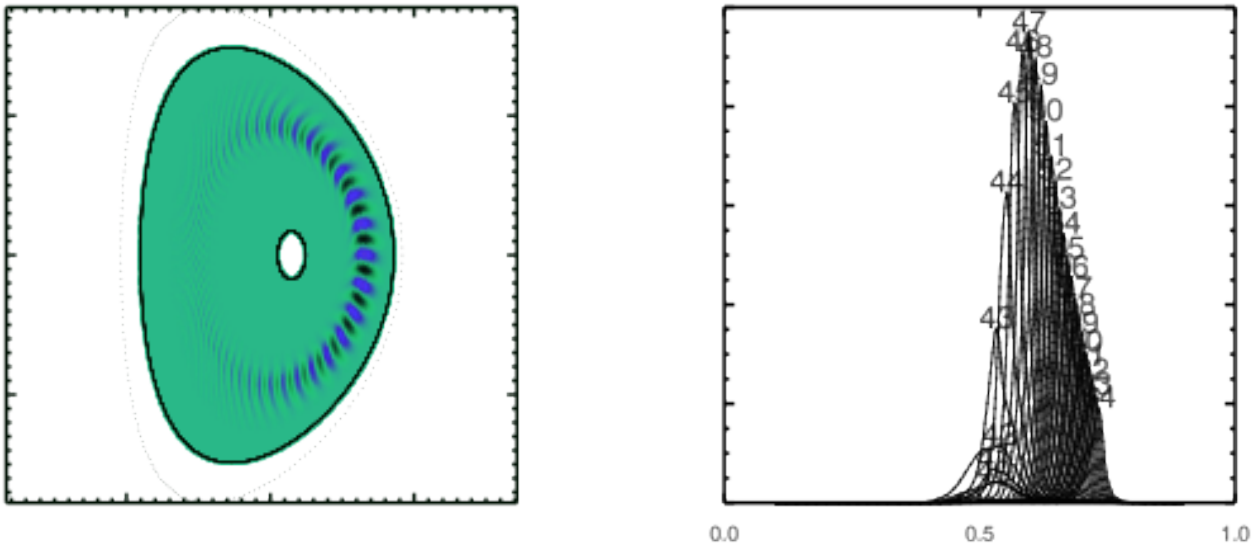

Figure 29: 2D contour (left) and poloidal harmonics versus radius (right) of n=23 electric potential for the steady state case at β_α=2.64%. The complex mode frequency is ω/ω_A = (0.37, 0.074)

Steady State equilibrium with beam ions

For the steady state equilibrium simulations are also run with the addition of another energetic particle species, a Deuterium beam species with an injection energy of 1 MeV and anisotropic pitch-angle distribution. With the beam species the equilibrium is unstable for a broad range of mode numbers at the nominal beam beta value of 0.71% (Fig. 30). Figure 31 shows beam beta scan for n=19 for the steady state case at the nominal alpha beta value of β_α=1.02%. Comparing results of Fig. 31 with Fig. 26, we observe that the beam ion destabilizing contribution is similar to that of alpha particles at the nominal ITER parameters. We also found that the anisotropy of the beam velocity distribution is not important.

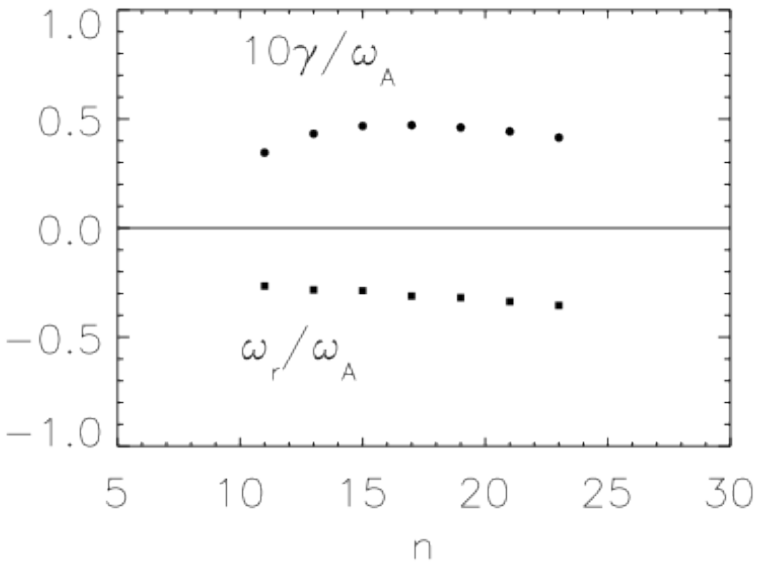

Figure 30: n-scan results for the steady state case at β_α=1.02%, βbeam=0.71%.

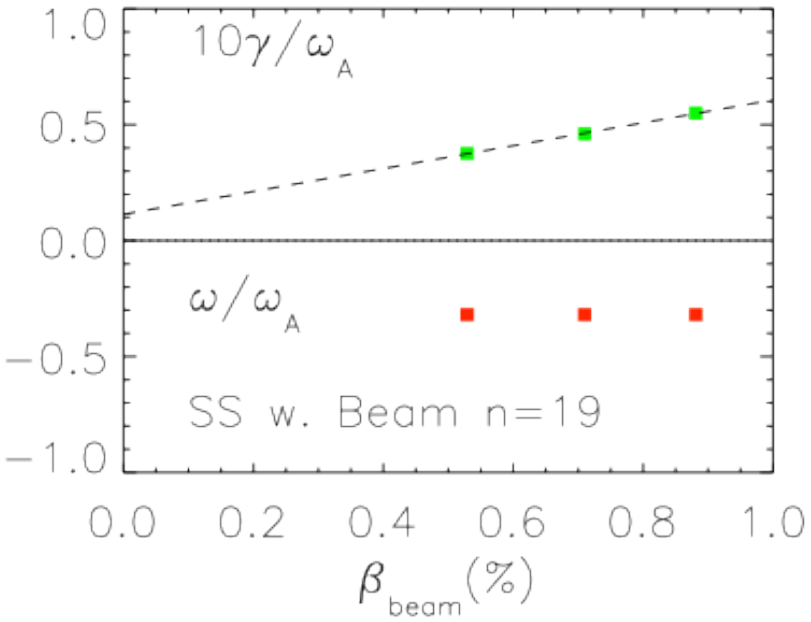

Figure 31: Beam beta scan for n=19 for the steady state equilibrium with deuterium beam. The alpha beta value is fixed at β_α=1.02%

4.5 GYRO

For the EP Milestone simulations with GYRO the ion species are fully gyrokinetic (realistic Larmor radius) and the electrons are drift kinetic (zero Larmor radius). The complete GYRO implementation of the gyrokinetic equations with δf fluctuations is described in Refs. [Candy03a, Candy03b, Candy10]. A hybrid time stepping algorithm treats the electrons implicitly and the ions explicitly. The electron mass is finite and set at $\mu_e \stackrel{\text{def}}{\equiv} \sqrt{m_e/m_i} = 40$, close to the realistic value for this system. Since the fast parallel electron dynamics are skipped over by the implicit time step, all large values of μ_e are functionally equivalent. All kinetic species, including the electrons, use prescribed radial density and temperature distributions in the evolution equations. The thermal ions are represented by a single D-T hybrid species (m_i=2.5m_p). The equilibrium velocity distribution for thermal species is an isotropic Maxwellian, specified as is appropriate for local equilibrium parameters. The alpha particles use the classical isotropic slowing down distribution appropriate for a birth energy of 3.5 MeV and a uniform crossover energy of E_c=0.2304 for the hybrid case and E_c=0.3249 for the steady-state case. By default, GYRO uses a crossover energy appropriate for the local parameters, but the uniform E_c model here is implemented for purposes of comparison with other codes in the milestone. The slowing down form implemented does not include broadening by pitch-angle scattering, but the contribution to $\partial f/\partial E$ on the finite grid point nearest the discontinuity at the birth energy is accounted for. Collisions and rotation are not included in the δf evolution for this study.

The equilibrium is specified with the complete Miller model. The shaping coefficients, toroidal flux, and q profile are given manually and the Miller model specifies the local variation (essentially $q(\theta)$) to ensure a local Grad-Shafranov equilibrium everywhere. This solution involves the local beta gradient. For purposes of this study, the beta gradient is held fixed at the nominal classical value even when the driving alpha density is changed from the classical prediction.

We now briefly describe GYRO results from the alpha-driven milestone benchmark cases. Both cases were run using 550 radial grid points over a radial domain of approximately $0.16 \le r/a \le 0.80$, adequate to resolve global ITG modes and well above the requirements for AEs with the given range of magnetic shear. The typical GYRO velocity-space resolution of an 8×8 energy and pitch angle grid is used. This resolution is converged to within a few percent for global mode linear growth rate and a fraction of a percent for real frequency. We also use standard resolution along field lines shown to be well converged for slowly varying envelope functions and all but the most extreme flux surface shaping. All eigenmodes calculated here fall well within these requirements. GYRO is spectral in the toroidal direction, and linear results here consider one toroidal n number at a time.

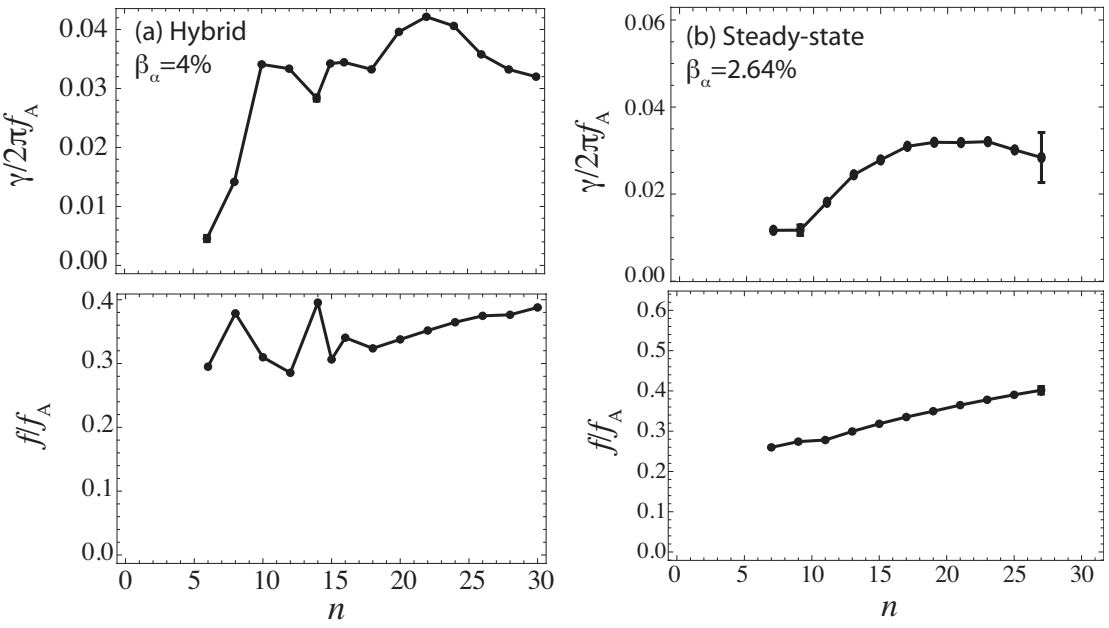

Fig. 32: The linear growth rate and frequency vs. n normalized to the Alfvén transit time for (a) the hybrid case at $\beta_\alpha(0)$=4% and (b) the steady-state case at $\beta_\alpha(0)$=2.64%.

Figure 32 shows a scan in toroidal n number for each ITER case. The core alpha beta values ($\beta_\alpha(0)$=4% for hybrid and ($\beta_\alpha(0)$=2.64% for steady-state) are well above threshold. These cases do not include neutral beam drive. We note that the hybrid case shows three distinct peaks representing distinct Alfvén branch modes competing for dominance. The steady-state case appears to be dominated by a single mode. Both show peak linear drive near n=20. The projected global linear threshold of the n=19 global mode is illustrated for each case in Fig. 33. For each case, the classical alpha profile has a peak beta of $\beta_\alpha(0) \approx 1\%$. The predicted hybrid threshold of $\beta_\alpha(0) = 1.3\% > 1\%$ indicates alpha particles alone do not drive AEs unstable in that scenario. By contrast, the projected steady-state case threshold of

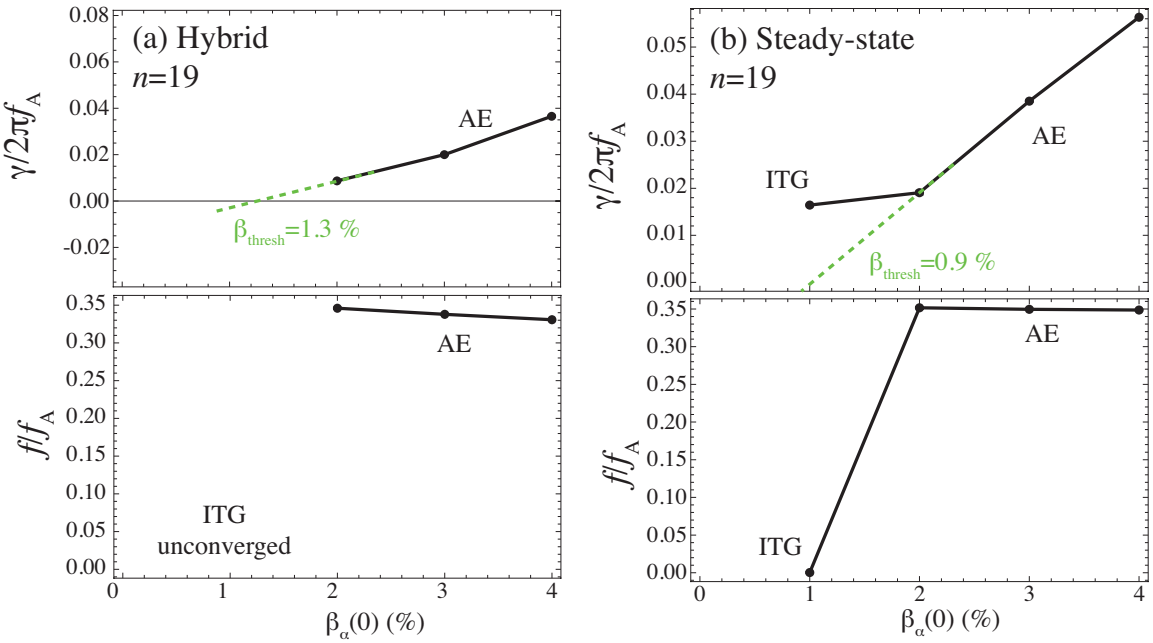

Fig. 33: The linear growth rate and frequency at n=19 vs. $\beta_\alpha(0)$normalized to the Alfvén transit time for (a) the hybrid case and (b) the steady-state case.

$\beta_\alpha(0) = 0.9\% < 1\%$ indicates this case to be unstable to global AEs even in the absence of beam ion drive, albeit weakly.

Figures 34 and 35 show eigenmodes at three representative n values from the scans of Fig. 32 for the hybrid and steady-state cases respectively. Most sampled eigenmodes exhibit the wide radial footprint, coupling of many poloidal harmonics, and ballooning behavior characteristic of global TAEs. The one exception is the n=15 eigenmode of the hybrid case. This case is dominated by a single poloidal harmonic and shows virtually no ballooning. Such behavior is more characteristic of a BAE (as in, for example, Bass E.M. and Waltz R.E., Phys. Plasmas 20, 012508 (2013)) or EPM.

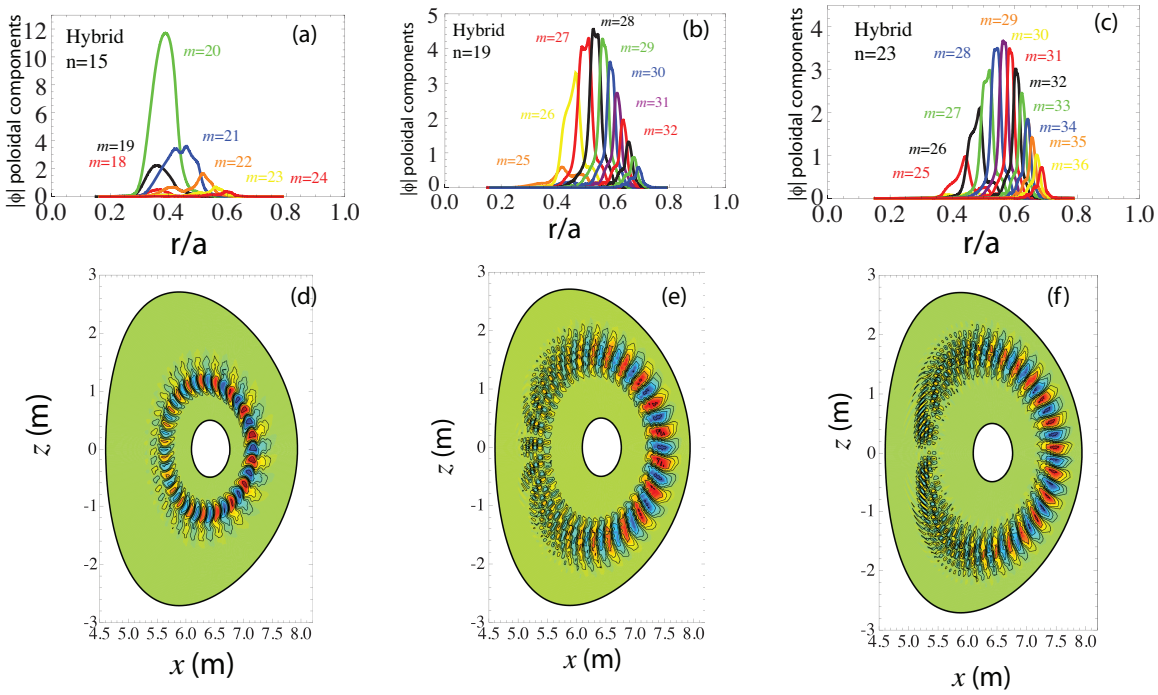

Fig. 34: Poloidal decomposition (a, b, and c) and contour plots (d, e, and f) of eigenfunctions of three representative n values from Fig. 32a for the hybrid case: n=15 (a and d), n=19 (b and e), and n=23 (c and f).

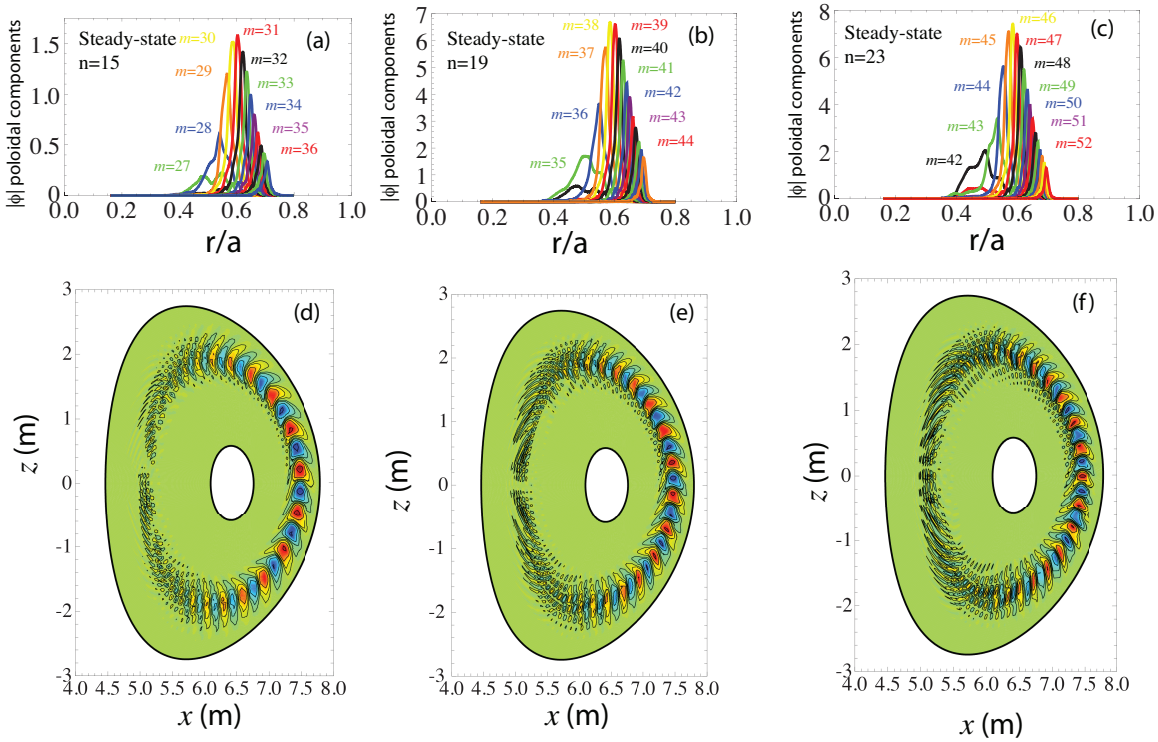

Fig. 35: Poloidal decomposition (a, b, and c) and contour plots (d, e, and f) of eigenfunctions of three representative n values from Fig. 32b for the steady-state case: n=15 (a and d), n=19 (b and e), and n=23 (c and f).

4.6 GTC

For this joint study, a toroidal mode number scan and a beta alpha scan of the toroidicity-induced Alfven eigenmode(TAE) were performed for a hybrid scenario equilibrium and a steady state equilibrium using Gyrokinetic Toroidal Code(GTC) [Lin98]. The thermal ions are treated gyrokinetically using a Maxwellian distribution function. To treat electrons, the electron distribution function is expanded using the smallness parameter of the ratio of wave frequency to electron transit frequency [Holod09]. In the zeroth order, the electrons can be considered a massless fluid and solved using the electron continuity equation. Non-adiabatic responses are treated kinetically in the higher order. The GTC code has been applied recently to simulate beam-driven TAEs in DIII-D plasmas [Wang13].

For this study only adiabatic electrons are considered. To treat the alpha particles more realistically, an isotropic slowing down fast alpha particle distribution was implemented into GTC. The results are presented below.

Hybrid Equilibrium

Figure 36 shows the hybrid scenario n=19 TAE frequency and growth rate of the for different values of the on axis alpha beta. When alpha beta is adjusted, the TAE frequency remains approximately constant near $\omega=0.031\omega_A$. The n=19 TAE has an alpha beta threshold of approximately $\beta_{\alpha 0}=1\%$. In Figure 37, a toroidal mode number scan is shown for an alpha beta of $\beta_{\alpha 0}=4\%$. While growth rate for the different toroidal mode numbers were similar, the n=19 mode growth rate is slightly larger. The TAE mode structure for the different toroidal mode numbers scanned are shown in Figure 38, and the poloidal harmonics of the modes are shown in Figure 39. The mode structures are all broad and include many m-harmonics.

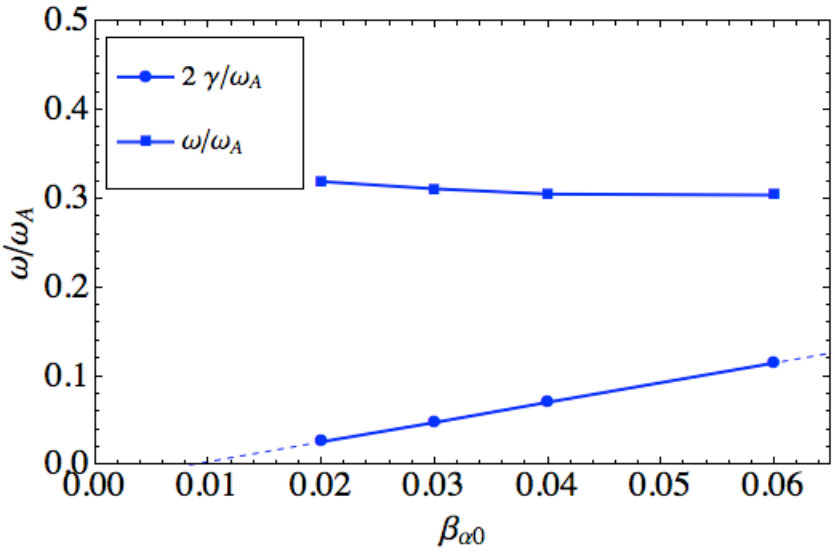

Figure 36: TAE growth rate and frequency for the hybrid equilibrium are plotted vs. the on axis alpha beta. A line of best fit for the growth rate drawn as the dashed line is projected to find the alpha beta threshold.

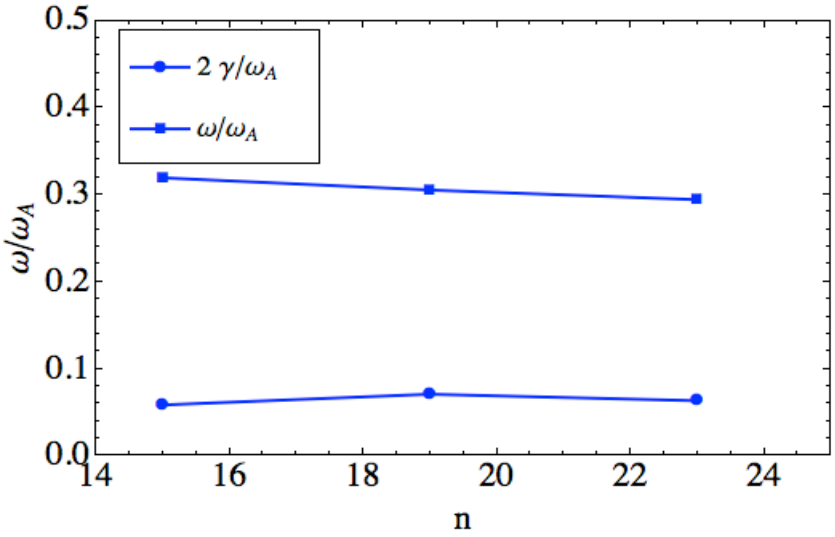

Figure 37: TAE growth rate and frequency for the hybrid equilibrium are plotted vs. toroidal mode number with an alpha beta $\beta_{\alpha 0}$=4%.

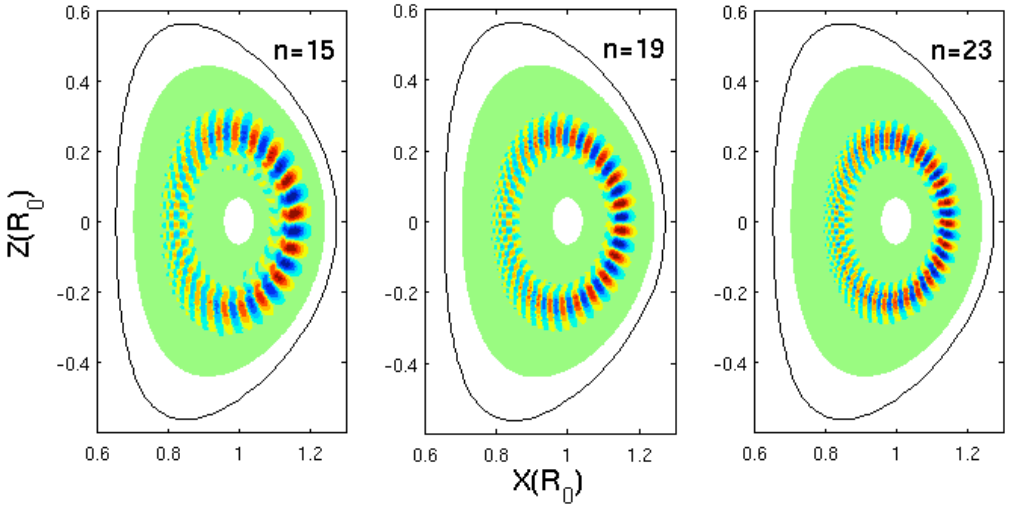

Figure 38: The hybrid scenario electrostatic potential for toroidal mode numbers n=15,19,23 are plotted. The last closed flux surface is shown by a solid black line, and white space represents outside of the simulation domain.

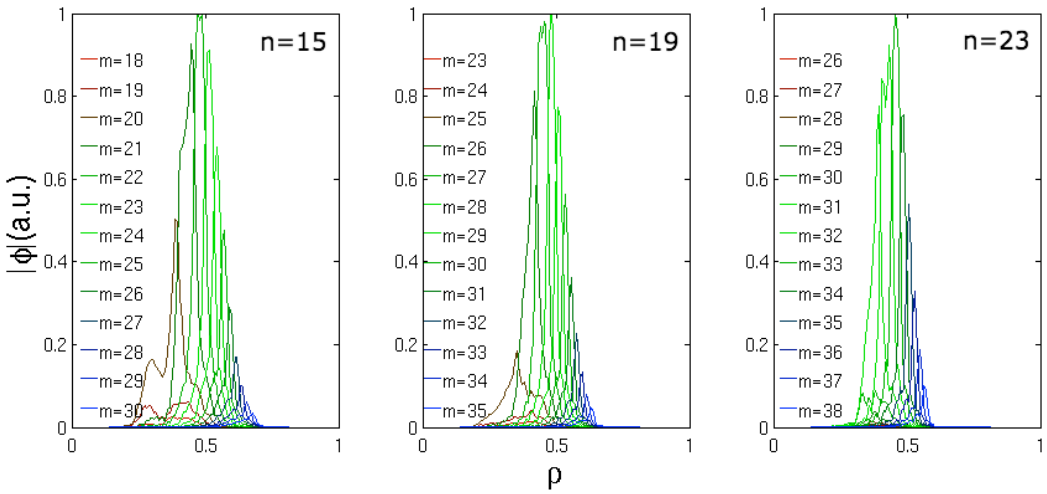

Figure 39: The poloidal harmonics of the TAE in the hybrid equilibrium with toroidal mode numbers n=15,19,23 are plotted.

Steady state equilibrium

Figure 40 shows the steady state n=19 TAE frequency and growth rate for different values of the on axis alpha beta. The growth rate has an on axis alpha beta threshold of slightly less than the hybrid scenario with a threshold of $\beta_{\alpha 0}$=0.7%. In Figure 41, the toroidal mode number scan is shown for an alpha beta of $\beta_{\alpha 0}$=4%. Like the

hybrid scenario, the growth rate of the n=19 TAE mode has a slightly larger growth rate. The steady state equilibrium TAE mode structure for the different toroidal mode numbers scanned are shown in Figure 42, and the poloidal harmonics of the modes are shown in Figure 43. The mode structure of the n=15 and the n=19 modes have dominant harmonics at the q-profile minimum. The mode structure of the n=23 TAE is shifted radial outward from the q-profile minimum.

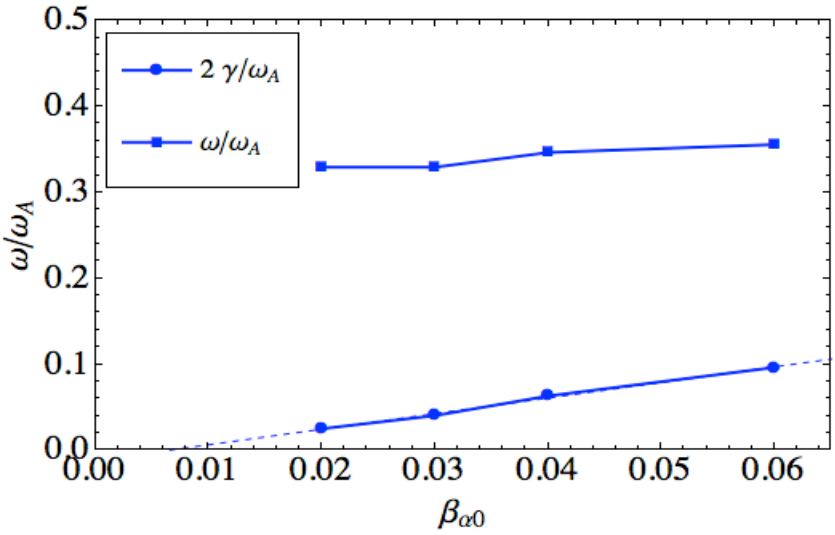

Figure 40: TAE growth rate and frequency for the steady state equilibrium are plotted vs. toroidal mode number with an alpha beta $\beta_{\alpha 0}$=4%.

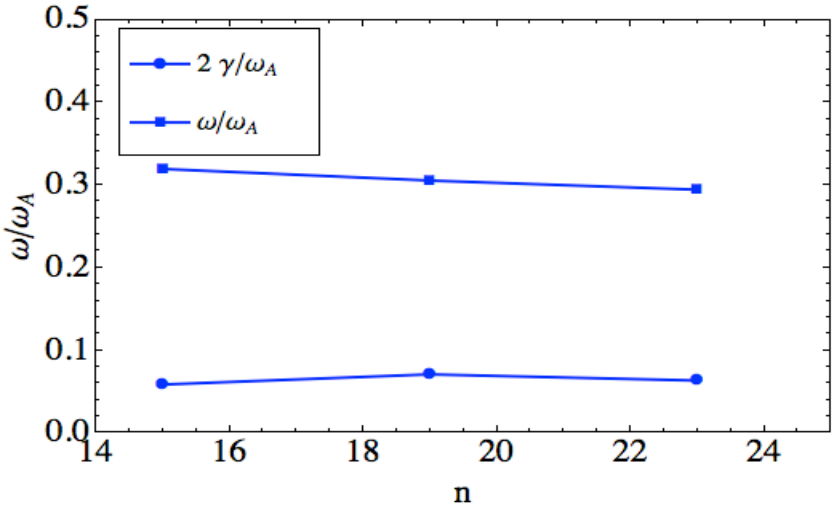

Figure 41: TAE growth rate and frequency for the steady state equilibrium are plotted vs. the on-axis alpha beta. A line of best fit for the growth rate which is drawn as the dashed line is projected to find the alpha beta threshold.

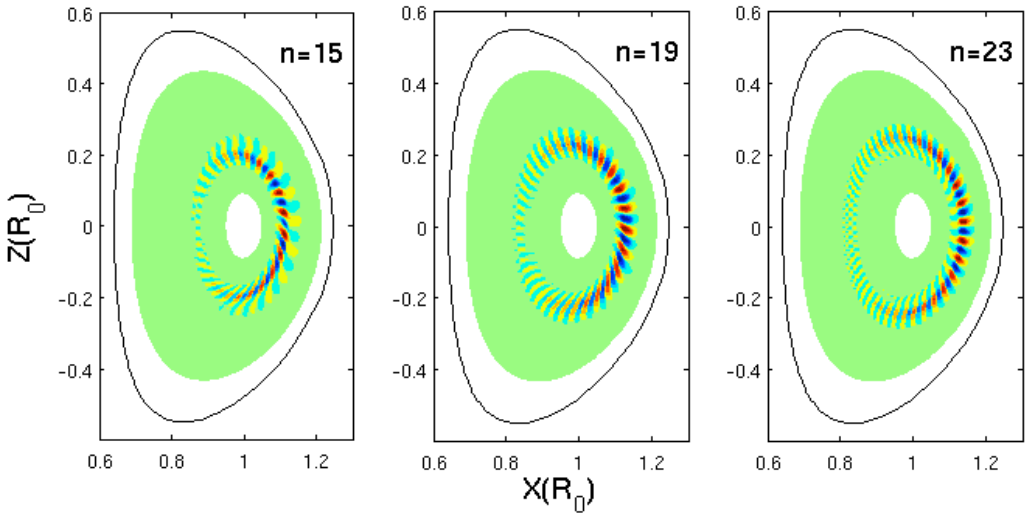

Figure 42: The steady state scenario electrostatic potential for toroidal mode numbers n=15,19,23 are plotted. The last closed flux surface is shown by a solid black line, and white space represents outside of the simulation domain.

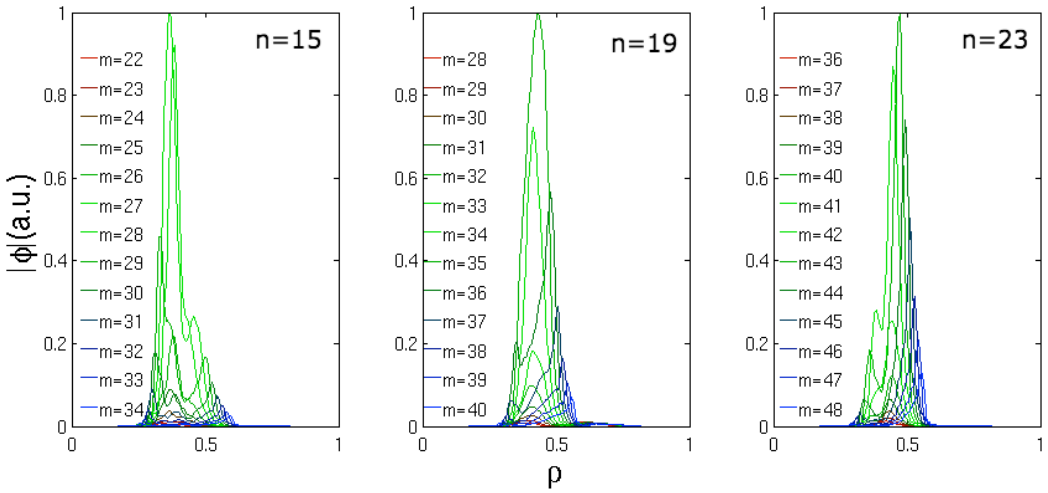

Figure 43: The poloidal harmonics of the TAE in the steady state equilibrium with toroidal mode numbers n=15, 19, 23 are plotted vs. the normalized square root of the toroidal flux. The minimum of the q-profile is located at ρ=0.4.

5 Nonlinear Simulations

5.1 GEM

Nonlinear simulations have been carried out for the Steady State equilibrium with beam ions to assess the nonlinear saturation amplitude and the effect on the alpha particle distribution. These nonlinear simulations use a grid resolution of (nx,ny,nz)=(512,32,64) in the field-aligned coordinates, 8 particles per cell per ion species, for the three ion species: thermal ions, alpha particles and the beam ions. Only the Fourier component of the selected single n is retained in the fields ϕ and $A_{||}$, but all Fourier components that are multiples of n are retained in the ion distribution. Following the initial linear growth the single-n mode saturates (Figure 44) due to the energetic particles (alpha and beam) trapping in the wave field and the generation of the n=0 component in the EP density fluctuation, which flattens the EP density profile and reduces the instability drive (Figure 45). A pitch-angle collision with the collision rate ν=10 rad/s is included for both alphas and the beam particles. On the simulation time scale (<0.5ms) this collision rate is too small to have any effect. The magnetic field fluctuation at the mode location r/a=0.6 is δBr/B~0.001. Attempt to run the simulation for longer time is prohibited by a thermal species density and temperature driven mode, which eventually becomes dominant in the initial value simulation. This thermal species driven instability is located near r/a=0.6, with a growth rate of ω/ω_A = (~0, 0.007), much weaker than the EP driven mode. The instability continues to grow after the EP driven mode saturates, eventually causes the simulation to terminate. We suspect that the thermal mode is a drift wave, which usually saturates due to coupling to other such waves and the zonal flow mode. Since these mechanisms are not included in the single-n nonlinear simulation, the saturation amplitudes of both the EP driven mode and the thermal mode over the collisional time scale (much longer than 0.3ms) are not determined by the present single-n simulation. What we can conclude from the simulation is that the initial saturation level of the EP driven mode is already large, $\delta B_r/B$~0.001, which causes significant relaxation of the alpha density profile.

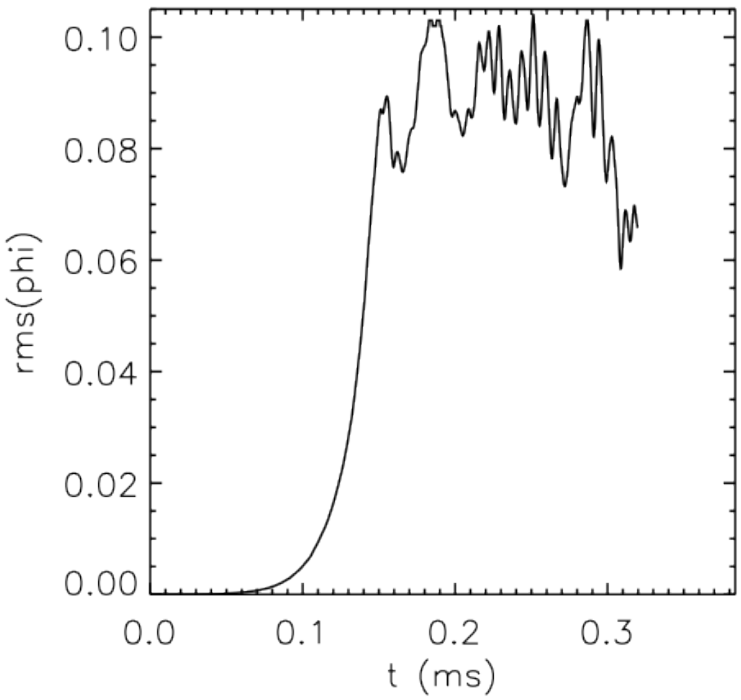

Figure 44: Nonlinear evolution of the root-mean-square of the electric potential of the n=19 mode for the Steady state equilibrium with Deuterium beam. β_{α}=1.02%, β_{beam}=0.71%.

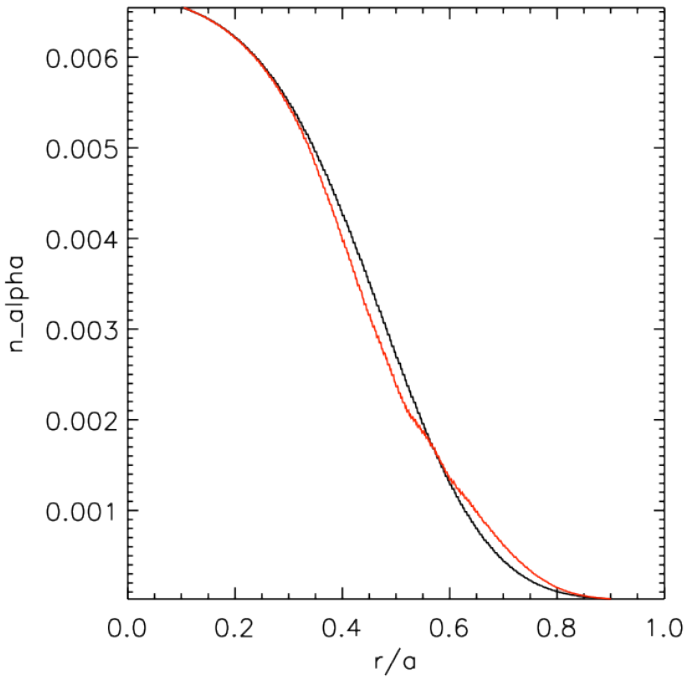

Figure 45: Initial (black) and final (red) alpha density profiles for the Steady state equilibrium with Deuterium beam. The alpha profile is significantly redistributed by the single n=19 mode.

5.2 M3D-K

Nonlinear simulations of the n=19 TAE are also carried out for the ITER steady state case using M3D-K. Only alpha particle drive is included. Higher alpha beta values are used in order to study the scaling of saturation level versus linear growth rate. Figure 46 shows the nonlinear evolution of the n=19 TAE at $\beta_\alpha(0)$=2% without particle collisions and without source and sink. The mode amplitude saturates initially before it decays. A longer simulation was not done because there were no effects of particle collisions and source/sink necessary to establish a physical steady state saturation. Also only particle nonlinearity was included for simplicity. Figure 47 shows the initial saturation level as a function of the linear growth rate. The result indicates that the saturation level scales approximately as $\delta B_r \sim \gamma^2$ for relatively small growth rates. This suggests that the wave particle trapping is the dominating saturation mechanism. Finally we note that the calculated saturation level at γ/ω_A ~4.5% is similar to that of GEM.

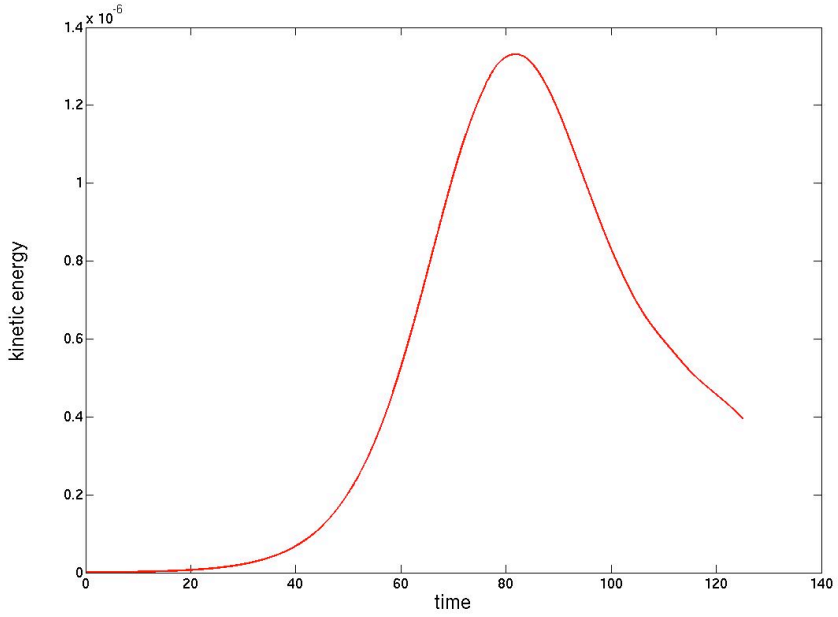

Fig. 46 Evolution of plasma kinetic energy of the n=19 TAE at $\beta_\alpha(0)$=2.0%.

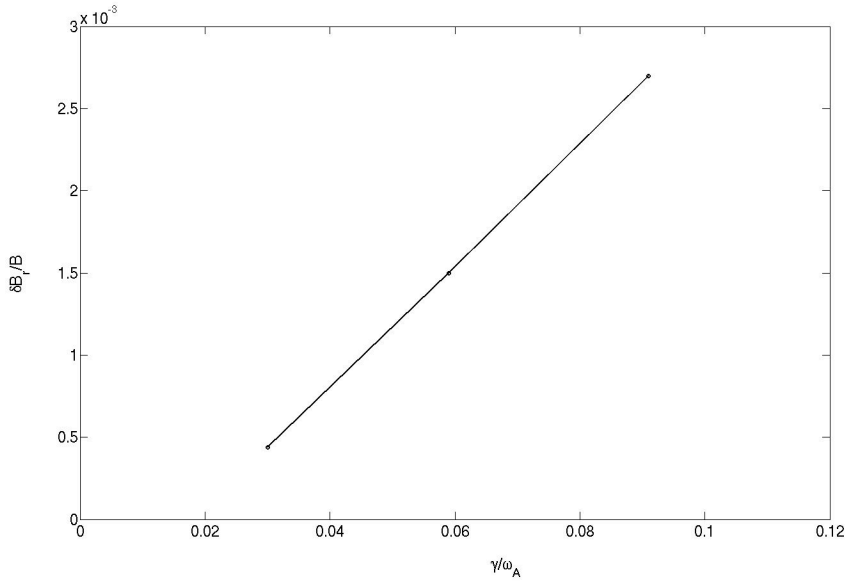

Fig. 47 Initial saturation level of radial magnetic field versus the linear growth rate of the n=19 alpha-driven TAE for the ITER steady state case.

6. Conclusion

Systematic linear and nonlinear simulations of alpha-driven TAEs in ITER have been carried out using six codes including three gyrokinetic codes, GEM GTC and GYRO, as well as the hybrid code M3D-K, the gyro-fluid code TAEFL, and the linear kinetic stability code NOVA-K. Two ITER equilibria are investigated including a hybrid scenario case with nearly flat q profile in the core and q(0)=1.2 and a steady state scenario case with a strongly reversed q profile and q_{min}=1.8. Both alpha particle and beam ion drives are considered. The results show that, with alpha particle drive alone, the hybrid case is stable to high-n TAEs whereas the steady state case is weakly unstable. With additional drive from beam ions, the steady state case is found to be strongly unstable to high-n TAEs with a broad unstable mode spectrum around n=17. The initial single-n nonlinear simulations of the steady state case show a significant fluctuation level and a considerable redistribution of alpha particle distribution near edge. It is conjectured that multiple unstable TAEs in the steady state scenario will drive strong redistribution of alpha particles and beam ions and can lead to significant energetic particle losses when coupled to edge loss mechanisms such as magnetic field ripple and/or 3D edge magnetic perturbations.

References

[Budny12] R.V. Budny, Nuclear Fusion 52 (2012) 013001

[Budny13] R.V. Budny, Xingqiu Yuan, S. Jardin, G. Hammett, B.A. Grierson, G.M. Staebler, J.E. Kinsey and JET EFDA Contributors, EPS meeting Espoo, June, 2013.

[Candy03a] J. Candy and R. E. Waltz, Phys. Rev. Lett. **91**, 045001 (2003)

[Candy03b] J. Candy and R.E. Waltz, J. Comput. Phys. **186** (2003) 545.

[Candy10] J. Candy and E.A. Belli, *GYRO Technical Guide*, General Atomics Report GA-A26818 (2010)

[Chen07] Y. Chen and S.E.Parker, J. Comp. Phys. 220, 839 (2007)

[Chen13] Y. Chen, T. Munsat, S.E. Parker et. al., Phys. Plasmas 20, 012109 (2013)

[Cheng86] C. Z. Cheng, M. C. Chang, Phys. Fluids 29 (1986) 3695.

[Cheng92] C. Z. Cheng, Phys. Reports 211 (1992) 1.

[Fu93] G. Y. Fu, C. Z. Cheng, K. L. Wong, Phys. Fluids B 5 (1993) 4040.

[Fu06] G. Y. Fu, W. Park, H. R. Strauss et al., Phys. Plasmas **13**, 052517 (2006).

[Fu12] G. Y. Fu et al., "M3D-K Simulations of Beam-Driven Alfven Modes in DIIID", 54th Annual Meeting of the American Physical Society Division of Plasma Physics, October 29–November 2, 2012; Providence, Rhode Island, invited talk, paper JI2.00003.

[Gorelenkov99] N. N. Gorelenkov, C. Z. Cheng, G. Y. Fu, Phys. Plasmas 6 (1999) 2802.

[Gorelenkov03] N. N. Gorelenkov, H. L. Berk, R. Budny et al., Nucl. Fusion **43** (2003) 594–605.

[Gorelenkov05] N. N. Gorelenkov, H. L. Berk, R. Budny et al., Nucl. Fusion **45** (2005) 226–237.

[Holod09] I. Holod, W. L. Zhang, Y. Xiao, and Z. Lin, Phys. Plasmas 16, 122307 (2009)

[Kramer06] G. J. Kramer, R. Nazikian, B. Alper et al., Phys. Plasmas 13 (2006) 056104.

[Lang10] J. Y. Lang, G. Y. Fu, and Y. Chen, Phys. Plasmas **17**, 4 (2010)

[Lang11] J. Y. Lang and G. Y. Fu, Phys. Plasmas **18**, 055902 (2011)

[Lin98] Z. Lin, T. S. Hahm, W. W. Lee, W. M. Tang, and R. B. White, Science 281, 1835 (1998).

[Liu13] D. Liu, G. Y. Fu, and J. A. Breslau et al., "M3D-K Simulations of Toroidicity-induced Alfven Eigenmodes on NSTX", 53th Annual Meeting of the American Physical Society Division of Plasma Physics, November 11-15, 2013; Colorado, Denver, contributed talk, paper JO4.00008.

[Poli12] F.M. Poli, C.E.Kessel, M. Chance, J. Manickam, S. Jardin, Nuclear Fusion 52 (2012) 063027

[Poli14] F.N. Poli, C.E. Kessel, P.T. Bonoli, D. Batchelor, R. Harvey, P. Snyder, Nuclear Fusion 54 (2014) 073007.

[Spong92] D. A. Spong, B. A. Carreras, C. L. Hedrick, Physics of Fluids **B 4** (1992) 3316.

[Spong94] D. A. Spong, B. A. Carreras, C. L. Hedrick, Physics of Plasmas **1** (1994) 1503.

[Spong12] D. A. Spong, E.M. Bass, W. Deng, W. W. Heidbrink, Z. Lin, B. Tobias, M. A. Van Zeeland, M. E. Austin, C. W. Domier, N. C. Luhmann, Jr., Phys. Plasmas 19 (2012) 082511-1.

[Spong13] D. A. Spong, Nuclear Fusion **53**, 053008 (2013).

[Spong14] D. A. Spong, Plasma and Fusion Research, Volume **8**, 3403077 (2014).

[Wang13] Z.X. Wang, Z. Lin, I. Holod et al., Phys. Rev. Lett. 111, 145003 (2013).

[Zeeland06] M. A. Van Zeeland, G. J. Kramer, M. E. Austing et al., Phys. Rev. Lett. 97 (2006) 135001.

Appendix ALPHA: Local 1D stiff AE transport model

In addition to participating in the milestone code comparison study, the GYRO team in the GSEP SciDAC project has focused considerable effort in developing a simple 1-dimensional unified predictive model for energetic particle density profiles limited by unstable Alfvén eigenmode (AE) transport. The model combines the GYRO-fitted quasilinear microturbulent transport model of Angioni [1] with a simple assumption of stiff AE transport that locks the *local* energetic particle gradient to a calculated *local* stiff transport threshold gradient. A similar model including only the effect of stiff AEs was implemented by Ghantous, et al. [2] to study NBI transport in DIII-D. Our model has been principally applied to alpha particles in ITER, but verification against an NBI-heated DIII-D case is also well underway. The model is implemented in the new ALPHA code.

We emphasize that the ALPHA model is conjectural and is meant as a tractable first prediction of AE limited alpha or NBI profiles to be tested against more sophisticated nonlinear predictions as they become available. A local critical-gradient model comes close to the "worst case" scenario, with some important caveats described below. As such, our results should be interpreted as an accessible estimate of the extent to which unstable AEs will pose a serious alpha confinement risk in ITER. For the ITER performance prediction of Kinsey [3] studied here, AE transport is found to be localized in the mid core with microturbulence controlling only nominal edge particle losses, mostly at low energies.

The ALPHA code includes the fusion source and the effective sink into a population of helium ash. It is assumed that the local classical slowing-down velocity-space distribution is maintained even as the alpha density is transported away from the (transport free) classical slowing down alpha density profile. The high-n micro-turbulent contribution to alpha transport is given by combining the known absolute energy flux appropriate to the Q=10 performance scenario in Ref. [3] with the Angioni et al. model [1] for the quasilinear ratio of energetic particle effective diffusivity to thermal plasma energy effective diffusivity. To the earlier Angioni et al. studies [4] of ITER alpha transport we add a *marginal stability* (or *stiff*) model for the alpha-driven AE transport. In this model, *locally* unstable AEs drive the alpha gradient to the *local* eigenmode alpha density gradient stability threshold determined by fully realistic GYRO [5] linear stability calculations. We report AE stability thresholds for the commonly used Maxwellian effective temperature alpha distribution, which we found to be indistinguishable within model error estimation from thresholds calculated using the classical slowing-down distribution. To clarify, the isotropic classical slowing-down "alpha" velocity distribution has a spectrum of energies from the 3.5 MeV fusion birth energy down to "zero" energy, but any alpha particle with energy less than the local plasma thermal particle energy can be identified as "helium ash".

For the Kinsey prediction [3] ITER *base case* profiles illustrated in Fig. 1 (distinct from the two cases studied under the EP milestone benchmark), GYRO calculations predict unstable AEs only over a fraction of mid-core radii near the peak in the slowing-down density gradient. If locally unstable AEs are restricted to the mid-core radii (and do not reach the plasma edge), the stiff AE transport only broadens the highly peaked slowing-down density profile. While the central alpha density is always less than the transport-free slowing-down density, the transported alpha density can elsewhere slightly exceed the local slowing-down density because of re-deposition. Both micro-turbulent and AE alpha mid-core transport flows peak at mid-radius. The mid-core AE transport flow is 3 to 5-fold larger than the micro-turbulent transport flow in the examples given. If the AE threshold is exceeded only in the mid-core, the micro-turbulent transport completely controls the net alpha loss to the edge; while broadening the alpha density profile, unstable AEs do not propagate to the edge to cause loss there. The edge particle loss fraction is highly dependent on the assumed edge boundary alpha density. In the worst case, when the boundary alpha density is zero, the fractional alpha particle loss amounts to only 7% per cent of volume total birth alpha particles. The net particle loss is an order of magnitude less (less than 1%) when the boundary alpha density is assumed to be the local slowing down density (in essential agreement with Ref. [5]).

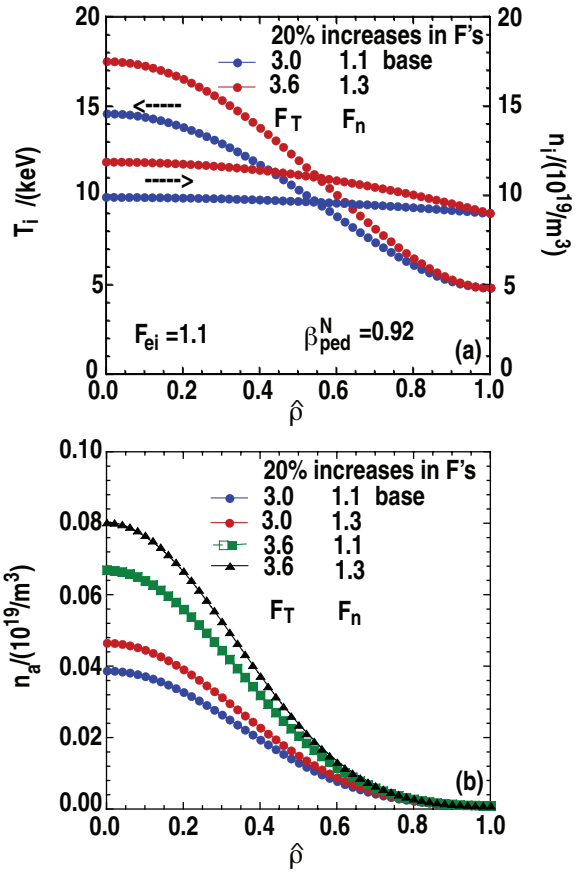

Fig. 1. The ITER *base case* ion temperature and (a) density radial profiles and (b) slowing-down alpha density radial profiles. Central increases with 20% increased temperature F_T and density F_n peaking factors indicated. $\hat{\rho} = 1.0$ corresponds to the H-mode pedestal top.

In detail, the ALPHA model finds a steady-state solution of the radial density evolution equation

$$\partial n_\alpha(r)/\partial t - 1/V'\partial[V' D_\alpha \partial n_\alpha(r)/\partial r]/\partial r = S_0(r)[1 - n_\alpha(r)/n_\alpha^S(r)] \qquad (1)$$

where $S_0 = n_D n_T \langle\sigma\upsilon\rangle_{DT} \sim (n_i^2/4)(T_i/10\ \mathrm{keV})^2 \langle\sigma\upsilon\rangle_{DT-10}$ is the fusion source with $\langle\sigma\upsilon\rangle_{DT-10} = 1.0\times10^{-22}$ $\mathrm{m^3 s^{-1}}$ at $T_i = 10$ keV to keep the scaling of the slowing down alpha density profile with T_{ped} and n_{ped} simple . The slowing down sink for

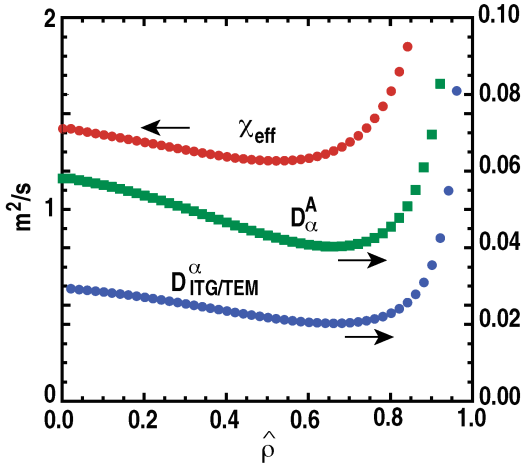

Fig. 2.Radial profiles of the effective thermal energy diffusivity χ_{eff} [provided by Eq. (5)] and (pinched) effective alpha particle diffusivity $D^{\alpha}_{ITG/TEM}$ (provided by Eq. [4(a-c)]) from high-n micro-turbulence. The roughly two-fold larger diffusive component D^{A}_{α} (provided by Eq. [4(b)]) also shown. $\hat{\rho} = 1.0$ corresponds to the H-mode pedestal top.

alphas, $S_0(r)[n_\alpha(r)/n^S_\alpha(r)] = n_\alpha(r)/\{\tau^S(r)I_2[a(r)]\}$, is also the source to the helium ash with the continuity equation

$$\partial n_{He}(r)/\partial t - 1/V'\partial[V' D_{He}\partial n_{He}(r)/\partial r]/\partial r = S_0(r)[n_\alpha(r)/n^S_\alpha(r)] \quad (2)$$

where $V' = d[2\pi^2 \kappa r R_0]/dr$ to a good approximation. At the edge $\hat{r} = r/a$ (actually the pedestal top) we take the density boundary condition $n_\alpha(a)/n^S_\alpha(a) = d_1$ with d_1 between 0 and 1. The pessimistic condition $d_1 = 0$ corresponds to an orbit loss time much less than the slowing down and transport time. It seems unlikely that $d_1 = 1$ (the condition used in Ref. [4]) is exceeded. Without transport $D_\alpha = 0 \Rightarrow n_\alpha(r) = n^S_\alpha(r)$. In the model, there is inner core transport where $n_\alpha(r) < n^S_\alpha(r)$ and outer core redeposition where $n_\alpha(r) > n^S_\alpha(r)$. A marginally stable AE alpha transport "diffusivity" is added to the high-n micro-turbulent effective diffusivity $D^{\alpha}_{ITG/TEM}$:

$$D_\alpha = D_{AE}(a/n_\alpha)[(-\partial n_\alpha/\partial r) - (-\partial n^{th}_\alpha/\partial r)]_{>0} + D^{\alpha}_{ITG/TEM} \quad (3)$$

where $(-\partial n^{th}_\alpha/\partial r)$ is the local linear AE density gradient threshold, and $[x]_{>0} = 0$ if $x < 0$. When $(-\partial n_\alpha/\partial r) > (-\partial n^{th}_\alpha/\partial r)$, $D_{AE} \geq 0.3\ \mathrm{m^2/s}$ is sufficient to drive the alpha density gradient close to the threshold and, as is characteristic of "stiff" critical gradient models, the resultant transport flows are insensitive to larger values.

The micro-turbulent transport of alphas and helium ash is provided by the Angioni et al. quasilinear models [1,4] fitted to several cross-verified gyrokinetic codes. The key formulas are repeated here for convenience:

$$\Gamma^{\alpha}_{ITG/TEM} = -D^{\alpha}_{ITG/TEM} dn_\alpha/dr = n_\alpha D^A_\alpha\left(1/L^\alpha_n + C^\alpha_p/R\right) \quad (4a)$$

$$D^A_\alpha = D_{He}[0.02 + 4.5(T_e/E_\alpha) + 8(T_e/E_\alpha)^2 + 350(T_e/E_\alpha)^3] \quad (4b)$$

$$C^\alpha_p = 3/2(R/L_{Te})\{1/[(1+1/\hat{E}_c^{1.5})\log(1+1/\hat{E}_c^{1.5})] - 1\} \quad (4c)$$

where typically $C_p^{\alpha} < 0$ indicates "pinching". The Helium ash transport is given by

$$\Gamma_{ITG/TEM}^{He} = -D_{ITG/TEM}^{He} dn_{\alpha}/dr = n_{He} D_{He}[1/L_n^{He} + C_p^{He}/R] \tag{4d}$$

where the helium pinch is $C_p^{He} = -2$. The base normalization has $D_{He} \sim \chi_{eff} = \chi_i + \chi_e$ corresponding the combined effective energy diffusivity of the thermal plasma χ_{eff}. There is some simulation-based evidence that the onset of AE critical gradient transport does not increase (and may slightly improve) transport in the thermal species (including helium) (Ref. [6]); hence, we have not included any increase here. Importantly, we compute χ_{eff} from the actual $P_a + P_{aux}$ power flows derived from the $P_{aux} = 30$ MW, $Q = 10$ *base case* input temperature and density profiles in Fig. 1(a) [$(F_T, F_n) = (3.0, 1.1)$]:

$$\begin{aligned} \chi_{eff} &= Q_r/[n(-dT_i/dr - dT_e/dr)/2] \sim Q_r/[n_i(-dT_i/dr)] \\ &= E_{\alpha}\Gamma_{\alpha}^{birth}(1+5/Q)/[n_i(-dT_i/dr)] \end{aligned} \tag{5}$$

where $\Gamma_{\alpha}^{birth}(r) = \int_0^r V'(\bar{r}) S_0(\bar{r}) d\bar{r} / V'(r)$ is the alpha birth source flux. We emphasize that although these *base case* profiles closely match the TGLF predicted profiles, we do not take χ_{eff} directly from the TGLF model. Figure 2 illustrates the effective diffusivities for the high-n micro-turbulent transport. As indicated, the alpha transport pinching reduced the effective transport by about one-half. The alpha particle diffusivities are 100-fold smaller than the thermal energy diffusivity.

Figure 3 shows the 1D transport prediction with stiff AEs using AE thresholds calculated with temperature-equivalent Maxwellian velocity distributions. The dominant toroidal n-numbers are typically 16 on the inner core and 24 on the outer. The most pessimistic boundary condition $n_{\alpha}(a)/n_{\alpha}^{s}(a) = 0$ corresponds to an instantaneous orbit loss. The

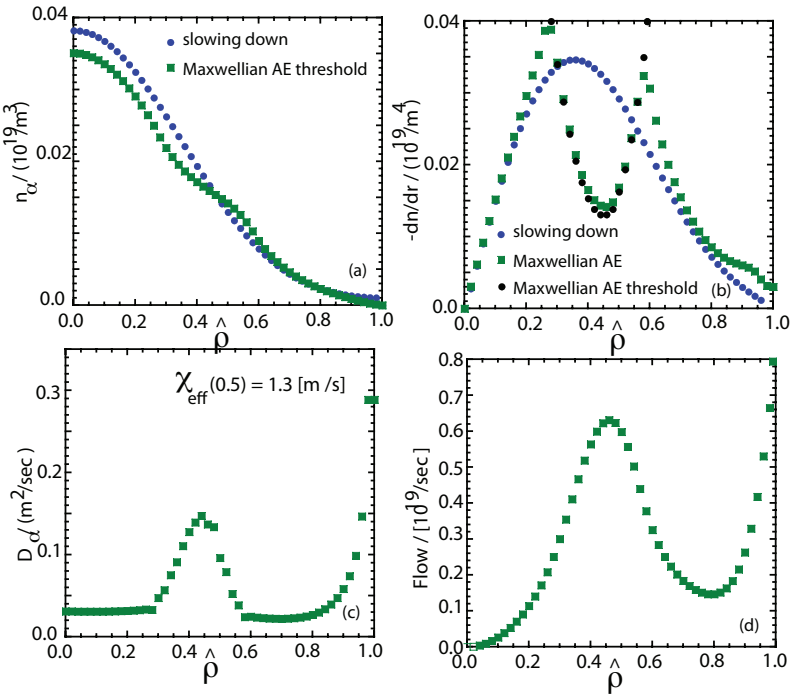

Fig. 3.Radial profiles of the (a) alpha density and the (b) alpha density gradient.Slowing down (without transport) shown with blue dots and transported with Maxwellian distribution AE thresholds with green squares.The Maxwellian AE local density gradient threshold profile is shown with black dots in (b). The corresponding effective (c) alpha particle diffusivity radial profiles and (d) the transport flows. $n_{\alpha}(a)/n_{\alpha}^{s}(a) = 0$. $\hat{\rho} = 1.0$ corresponds to the H-mode pedestal top.

7% alpha particle loss flow of 0.83×10^{19} s^{-1} [indicated by the O in Fig. 4(d)] out of a birth flow of 12×10^{19} s^{-1} is completely controlled by the micro-turbulent transport so long as the local AE thresholds are exceeded only the mid-core. The birth particle flow corresponds to 67 MW birth heating which is slightly more with 60 MW expected of the Q=10 and P_{aux} = 30 MW *base case* because the thermal profiles don't perfectly match Ref. [3] which included other losses. The alpha particle loss is reduced ten-fold (to 0.7%) with the boundary condition $n_a(a)/n_\alpha^s(a)=1$ [indicated by the X in Fig. 3(d)], consistent with Ref. [4]. The marginal stability AE transport merely broadens the slowing down alpha profiles with redeposition $n_\alpha(r)/n_\alpha^s(r)>1$ [Fig. 3(a)] and decreasing transport flow [Fig. 3(d)] $0.5<r/a<0.8$. Figure 3(b) indicates a kind of "avalanching" where the AE transport extends outside the region where $(-\partial n_\alpha^s/\partial r)>(-\partial n_\alpha^{th}/\partial r)$. The up-turn in the edge flow $0.8<r/a<1.0$ to the "O" in Fig. 3(d) in the case of $n_\alpha(a)/n_\alpha^s(a)=0$ is due to an increase in the net source by the decrease in the sink to helium $S_0(r)n_\alpha(r)/n_\alpha^s(r)\to0$ as $r\to a$. Solving the helium continuity equation Eq. (2) using the Angioni model Eq. 4(d), we find a very modest ash build-up $n_{He}(0)/n_i(0)=0.21\%(0.15\%)$ with (without) the helium pinch.

Figure 4 repeats Fig. 3 for the 20% increase in temperature and density peaking illustrated in Fig. 1(a): $F_T=3\to3.6$ and $F_n=1.1\to1.3$ with $F_{ei}=1.1$ and pedestal plasma parameters unchanged. The alpha birth rate and slowing down alpha density are doubled [comparing Fig. 1(b) and Fig. 4(a)], and Q is increased from 10 to 20 with injection still fixed at 30 MW. The peak plasma (alpha) beta is increased by 40% (100%) but the explicit plasma shaping (Shafranov shift, elongation) profile and q-profile are left unchanged. GYRO simulations have a built-in local MHD equilibrium [5], so there is a 50% increase in the so-called "MHD alpha" (total pressure gradient) stabilization. As indicated in Fig. 4(b), the slowing down alpha density gradient is doubled with the

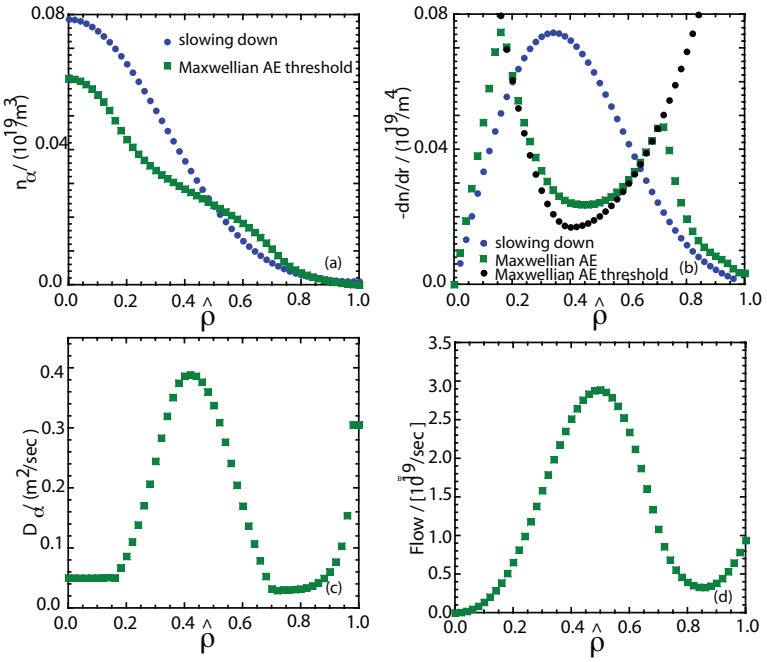

Fig. 4. The base case of Fig. 3 is repeated with the 20% increase in temperature and density peaking: $F_T=3\to3.6$ and $F_n=1.1\to1.3$ with $F_{ei}=1.1$ unchanged. Otherwise see caption Fig. 3.

alpha profile. As expected (neglecting the increased MHD-alpha stabilization), the Maxwellian AE threshold density gradient is largely unchanged [black dots in Fig. 4(b) vs. same in Fig. 3(b)]. The radial extent of AE instability increased. The peak mid-core AE particle flow increased about five-fold [comparing Fig. 4(d) with 3(d)] but most importantly the edge transport flow controlled by the micro-turbulent transport remains largely unchanged [0.9×10^{19}/s in Fig. 4(d) compared to 0.8×10^{19}/s in Fig. 3(d)]. Since the birth flows are doubled and the edge loss flow is unchanged, the fractional alpha losses (in particles and energy) are halved.

In our *ITER base case* examples, the AE redistribution of heating is confined to the mid-core. The losses to the edge are controlled by the high-n micro-turbulent transport, which transports only low energy particles so that $C << 1$. For the Angioni model $G_D(E)$, given by Eq. (32) and Fig. 2 of Ref. [1], has a strong cut-off for alpha energies above the energy $E > 33T_e$. From this model we find with edge pedestal $T_e = 5$ keV that $T_\alpha \sim 700$ keV , $\langle E \rangle \sim 1000$ keV$\sim 1/3 E_\alpha$, and $C \sim 1/33$ with the average energy of the transported particle around 30 keV, i.e. essentially hot helium. As noted in Ref. [4], fractional alpha heating losses via high-n turbulent transport are much lower than fractional birth alpha particle losses: in our example particle loss is between 7% and 0.7% but energy loss is $1/3\times1/33$ or roughly 100-fold smaller at between 0.7% and 0.07%.

From the illustrations provided for the given ITER *Q*=10 H-mode *base case* thermal plasma profiles, we conclude that the local AE mode linear threshold gradients are likely to be exceeded only in the mid-core, resulting in only modest re-deposition of alpha heating within the core. Clearly more work needs to be done on other ITER scenarios with significantly different *q*-profiles and in particular with flat *q*-profiles ($\hat{s} = 0$) out to mid-radius (in contrast to the case here). Reference [15] considered flat central *q*-profiles as well as *q*> 2 reversed shear ITER profiles, but consistently found alpha driven unstable global AE mode amplitude peaks were limited to the mid-core (25% to 60% of minor radius).

Comparison to DIII-D: Validation of ALPHA and nonlinear results

An effort to validate the ALPHA model against DIII-D discharges described in Ref. [7] is underway. The first preliminary studies use a threshold calculated in GYRO using an isotropic slowing down distribution. A more physical AE stiff transport threshold condition $\gamma_{\rm AE} = \gamma_{\rm ITG}$, as opposed to $\gamma_{\rm AE} = 0$ described in the ITER study above, is used in this validation effort. The less stringent AE critical gradient condition is motivated by nonlinear microturbulent suppression of AE transport observed in [6]. With this condition, the ALPHA model shows encouraging agreement with the experimentally observed profile, particularly with $n_\alpha(0)$. This verification study was performed considering only an isotropic heating beam. A generalization of GYRO to consider the anisotropy of the heating beam distribution is currently in the testing and debugging phase. The beam-heated ITER steady-state

scenario described as part of this milestone effort is a focus of these testing efforts. To date, no reliable result including anisotropy can be reported.

Progress has also been made in nonlinear simulation of global profile flattening in the DIII-D verification cases. Saturated simulations including n=0 and n=3 show flattening in the vicinity of n=3 singular surfaces. Simulations including many harmonics of n=3 are planned for the near future.

[1] Angioni C. and Peters A.G., Phys. Plasmas 15, 052307 (2008)
[2] Ghantous K. et al., Nucl. Fusion 19, 092511 (2012)
[3] Kinsey J.E. et al., Nucl. Fusion 51, 083001 (2011)
[4] Angioni C. et al., Nucl. Fusion 49, 055013 (2009)
[5] Candy J. and Waltz R.E., Phys. Rev. Lett. 91, 045001 (2003); also Candy J. and Waltz R.E., J. Comp. Phys. 186, 545 (2003)
[6] Bass E.M. and Waltz R.E., Phys. Plasmas 17, 112319 (2010)
[7] Heidbrink W.W. et al., Fusion 53, 093006 (2013)
[8] Bass E.M. and Waltz R.E., Phys. Plasmas 20, 012508 (2013)